Tensile Stress-Strain Measurements of Nb_3Sn Superconducting Strands and Cables at Room Temperature

Submitted By
Elizabeth Buechler

In partial fulfillment of the requirements for the degree of

Bachelor of Science in Mechanical Engineering

Tufts University
School of Engineering
Medford, Massachusetts

May 2017

Committee:

Dr. Luisa Chiesa
Associate Professor, Tufts University
Department of Mechanical Engineering
Research Advisor

Dr. Gary Leisk
Senior Lecturer and Research Assistant Professor, Tufts University
Department of Mechanical Engineering

Abstract

Nb_3Sn is a composite low temperature superconductor that is used in high-field magnet applications such as nuclear fusion, high energy physics, and medicine. The material is formed by diffusion during a heat treatment process, after which it becomes extremely brittle. During magnet operation, Nb_3Sn strands experience loading conditions that may result in brittle fracture of the superconducting filaments or the entire strand. Additionally, axial, transverse, and bending strain that result from these loading conditions can limit the critical current of the strand. Therefore, characterization of the stress-strain behavior of Nb_3Sn is required to optimize the electrical and mechanical performance of magnets.

The objective of this study was to determine the mechanical properties of superconducting samples for Mevion Medical Systems, a provider of superconducting synchrocyclotrons for proton therapy cancer treatment. Tensile tests were performed on reacted and unreacted strands and cables at room temperature (300 K), according to standard test procedures. Custom sample grips were designed for testing twisted 5-strand cables. The Young's modulus from loading and unloading, yield strength, and strength at fracture were calculated for different sample types. The measured properties of the strands showed good agreement with literature values for similar materials. Analytical models on the mechanics of wire ropes were used to validate the empirical values for the Young's modulus of the cables. Overall, measurements of the unloading modulus exhibited smaller variation than measurements of the loading modulus and closer

agreement with the analytical solutions, suggesting that the unloading modulus may be a more accurate measure of the Young's modulus of the material. Observations from testing indicate certain limitations of the tensile testing apparatus and future areas of improvement. The measured mechanical properties of the Nb_3Sn materials can be used by Mevion to improve magnet design in proton therapy systems.

Acknowledgements

I would like to acknowledge all of the people who contributed their time and knowledge to the completion of this research project. First of all, I would like to thank my advisor, Professor Luisa Chiesa for all her guidance, advice, and support. She has taught me a great deal about designing experiments, analyzing results, and investigating a research question. Gaining exposure to laboratory research has helped shape my goals for pursing a graduate degree and a career in research, and I am grateful for the opportunity.

I would like to thank Federica Pierro, who spent many hours in the lab with me performing experiments. She was a constant source of advice and helped me overcome various challenges throughout the project.

Thank you to Dr. Gary Leisk and Dr. Makoto Takayasu for their valuable advice on experiment design and data analysis. I am also grateful to the other members of the Superconductivity Lab, Nate Allen and Zijia Zhao, for their assistance.

Finally, I would like to thank my family for their constant support. They have always encouraged me to pursue my goals and taught me the value of dedication and hard work.

Table of Contents

Abstract ii
Acknowledgements iv
Table of Contents v
1. Introduction 1
1.1 Thesis Objective 1
1.2 Background on Superconductors 2
1.3 Superconductor Applications 5
1.3.1 Nuclear Fusion Reactors 5
1.3.2 Nuclear Magnetic Resonance Spectroscopy 6
1.3.3 Particle Accelerators and Proton Therapy 7
1.4 Nb_3Sn Superconductors 10
1.4.1 Structure and Manufacturing 10
1.4.2 Effect of Strain on Magnet Performance 12
1.4.3 Tensile Testing 13
1.5 Thesis Scope 14
2. Experimental Methods 16
2.1 Test Samples 16
2.2 Tensile Testing Apparatus and Data Acquisition System 19
2.3 Sample Grip Design 21
2.4 Experimental Procedure 24
2.5 Data Post-Processing 27
2.5.1 Calculation of Stress and Strain 27
2.5.2 LVDT Calibration 28
2.5.3 Calculation of Mechanical Properties 29
2.5.4 Uncertainty Analysis 32
3. Experimental Results and Discussion 35
3.1. Reference Material: Copper Strand 35
3.2 Reacted Nb_3Sn Strands 39
3.3 Unreacted Nb_3Sn Strands 41
3.4 Reacted Nb_3Sn Cables 44
3.5 Unreacted Nb_3Sn Cables 45
3.6 Discussion and Summary of Experimental Results 47
4. Analytical Results and Discussion 52

4.1 Model 1: Costello and Phillips....53
4.2 Model 2: Wu and Cao....57
4.3 Discussion of Analytical Results....60
5. Conclusions....62
5.1 Future Work and Recommended Improvements to the Tensile Testing Apparatus....63
6. References....66
7. Appendix A: Sample Grip Drawings....68
8. Appendix B: Stress-Strain Plots for Mevion Samples....75
8.1 Reacted Strands....75
7.2 Unreacted Strands....76
8.3 Reacted Cables....76
8.4 Unreacted Cables....78

List of Figures

Figure 1: Critical surface of a superconductor defined in terms of the critical temperature (T_c), critical magnetic field (B_c), and critical current density (J_c) [3]. 3
Figure 2: Cross-section of Nb_3Sn strands manufactured with the (a) internal tin and (b) powder-in-tube processes [5]. 11
Figure 3: Nb_3Sn samples from Mevion: (a) unreacted cable, (b) reacted cable, (c) unreacted strand, and (d) reacted strand. 17
Figure 4: Cross-section of the reacted cable with dimensions specified by Mevion. 17
Figure 5: Overall model of tensile testing apparatus (left) and close up of sample area showing the extensometers mounted on a strand (right). 20
Figure 6: Sample gripping methods recommended by IEC Standard 61788-6 for the tensile testing of reacted Nb_3Sn strands [15]. 22
Figure 7: Design of the sample grips used for strand measurements: (a) top sample grip, (b) bottom sample grip, and (c) v-groove cross-section of the sample grips. Units are in inches. 23
Figure 8: Design of the sample grips for the cable measurements: (a) top sample grip, (b) bottom sample grip, and (c) cross-section of the cable and v-groove. Units are in inches. 24
Figure 9: Placement of sandpaper in the lower sample grip for strand measurements. 26
Figure 10: (a) Mean (curve) and standard deviation (error bars) of the stress-strain curves for the copper strands and (b) a stress-strain curve for sample #11. 37
Figure 11: Stress-strain curve of a copper strand, showing the effect of slack in the tensile testing apparatus at the point of unloading. 38
Figure 12: (a) Mean (curve) and standard deviation (error bars) of the stress-strain curves for the reacted Nb_3Sn strands and (b) a stress-strain curve for reacted Nb_3Sn strand #4. 41
Figure 13: Stress-strain curve of (a) a non-straightened (wavy, bent, and twisted) and (b) a pre-straightened unreacted Nb_3Sn strand. 43
Figure 14: (a) Mean (curve) and standard deviation (error bars) of the stress-strain curves for the reacted Nb_3Sn cables and (b) a stress-strain curve for reacted cable #4. 45
Figure 15: Mean (curve) and standard deviation (error bars) of the stress as a function of strain for the unreacted cables and (b) the stress-stain curve for unreacted cable #2. 47
Figure 16: Comparison of the stress strain curves of a reacted strand, reacted cable, and unreacted cable. 50
Figure 17: (a) Geometric parameters of a reacted Nb_3Sn cable prior to loading and (b) a force-body diagram showing the forces acting on the cross-section of a side strand. 55
Figure 18: Mevion cable cross-section assuming circular cross-sections of the side strands. 58

List of Tables

Table 1: Critical temperature (T_c), critical magnetic field (B_c), and critical current density (J_c) of NbTi and Nb_3Sn [3]. 4
Table 2: Nb_3Sn samples tested for Mevion Medical Systems. 16
Table 3: Elemental systematic and random uncertainties of measurement devices obtained from manufacturer specifications. 32
Table 4: Characteristics of tested samples and calculated properties and notes on testing and sample fracture for each sample type. 35
Table 5: Mean, standard deviation, and coefficient of variation of E_o, E_u, and $S_{Y0.2\%}$ for the copper strands. 36
Table 6: E_o, E_u, and S_u for each reacted Nb_3Sn strand. 40
Table 7: Mean, standard deviation, and coefficient of variation of E_o, E_u, and S_u for the reacted Nb_3Sn strands. 41
Table 8: E_o and E_u for individual reacted Nb_3Sn cables. 44
Table 9: Mean, standard deviation, and coefficient of variation for E_o and E_u for the reacted Nb_3Sn cables. 45
Table 10: E_o, E_u, and $S_{Y0.2\%}$ for the unreacted Nb_3Sn cables. 46
Table 11: Mean, standard deviation, and coefficient of variation of E_o, E_u, and $S_{Y0.2\%}$ for the unreacted Nb_3Sn cables. 46
Table 12: Summary of the mechanical properties of the reacted Nb3Sn strands, reacted Nb3Sn cables, and unreacted Nb3Sn cables. 48
Table 13: Δ_a for the reacted and unreacted cable samples. Calculations are based on the samples for which both E_o and E_u were measured. 49

1. Introduction

1.1 Thesis Objective

The objective of this research project was to determine the mechanical stress-strain behavior of Nb_3Sn superconducting strands and cables for Mevion Medical Systems [1], a medical device company in Littleton, MA. Mevion is a provider of superconducting synchrocyclotrons, a type of particle accelerator used in proton radiation therapy for cancer treatment. These devices require high magnetic fields that are produced by superconducting magnets made from Nb_3Sn. The company has requested the mechanical properties of the Nb_3Sn strands and cables used in their magnets at room temperature, which they will use to optimize magnet performance.

To determine these mechanical properties, tensile tests were performed on reacted and unreacted Nb_3Sn strands and cables at room temperature (300 K). The Young's modulus, yield strength, and strength at fracture were calculated from the measured data, and validated against analytical solutions. Although the results of this study only directly apply to the particular materials and cable configuration used by Mevion, the experimental methodology and analytical approach could be applied to superconductors in other applications.

1.2 Background on Superconductors

Superconductors are materials that exhibit both zero electrical resistance and perfect diamagnetism below a certain critical temperature (T_c), magnetic field (B_c), and current density (J_c). Zero electrical resistance of the material in the superconducting state allows current to flow with negligible resistive losses over time. Perfect diamagnetism is characterized by the expulsion of magnetic fields from the material in the superconducting state. This phenomenon, known as the Meissner Effect, was discovered in 1933 by Meissner and Ochsenfeld [2]. A magnetic field is induced within the superconductor that either partially or entirely cancels out the applied field. Superconductors are categorized as either Type I or Type II superconductors, depending on the characteristics of this field expulsion. For Type I superconductors, the magnetic field is entirely excluded from the material below the critical field B_c. For Type II superconductors, the magnetic field is partially excluded below a magnetic field B_{c2} and entirely excluded below a magnetic field B_{c1}.

Together, T_c, B_c, and J_c define the transition between the normal and superconducting states. These parameters are interdependent, and their relation is defined by the critical surface of the specific material, as shown in Figure 1. This critical surface describes the operational limits of a superconducting material, and must be considered when designing superconducting magnets for various applications.

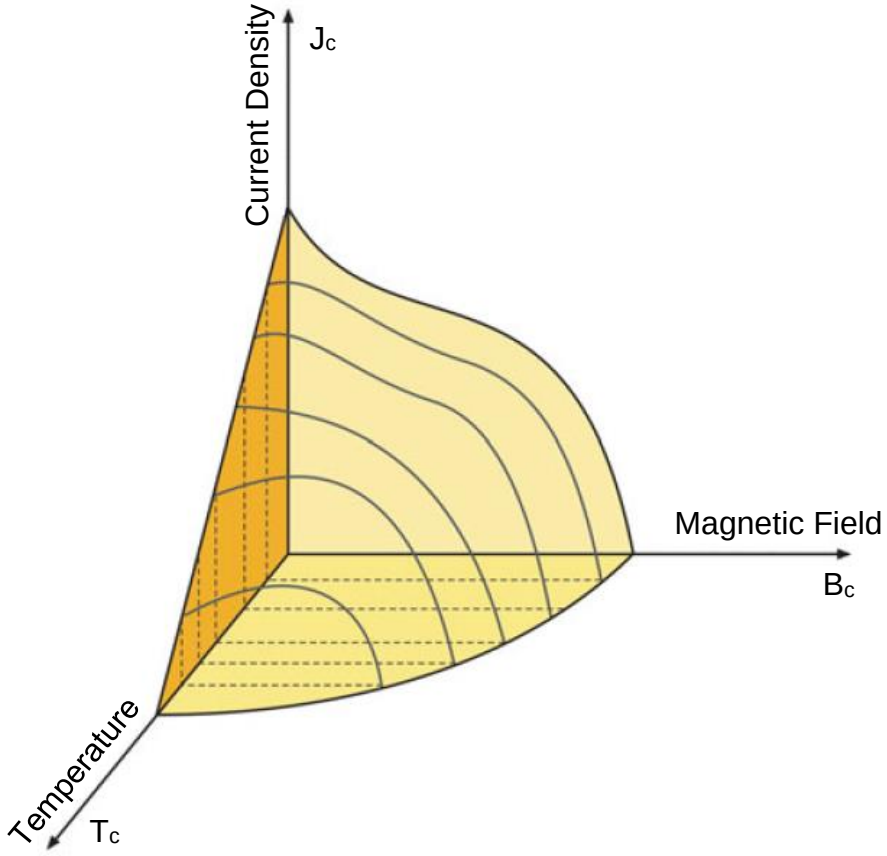

Figure 1: Critical surface of a superconductor defined in terms of the critical temperature (T_c), critical magnetic field (B_c), and critical current density (J_c) [3].

Superconductivity was first discovered in 1911 by Kamerlingh Onnes in mercury at 4.2 K [3]. Since then, thousands of different superconducting elements and compounds have been discovered. Superconductors are classified according to their critical temperature, as either low temperature superconductors (LTS) or high temperature superconductors (HTS). The boiling point of nitrogen (77 K) is generally used to distinguish between HTS and LTS conductors, based on their transition temperature. For most of the 20th century, all known superconductors were LTS, requiring the use of cryogens such as helium and hydrogen with very low boiling points. NbTi and Nb_3Sn have been the only LTS conductors produced

at a commercial scale, due to their relatively high critical temperatures and magnetic fields (Table 1). NbTi is an ideal material for electromagnets because of its relatively ductile behavior, which allows it to be used under large loading conditions. However, its use is limited to applications with magnetic fields lower than 9 T, due to the critical magnetic field of the material [3]. Nb_3Sn is currently the only superconductor that is widely used in applications that require higher magnetic fields, due to its high critical magnetic field and manufacturability.

Table 1: Critical temperature (T_c), critical magnetic field (B_c), and critical current density (J_c) of NbTi and Nb_3Sn [3].

	T_c (K)	B_c at 4.2 K (T)	J_c at 4.2 K (A/cm^2)
NbTi	9.3	11	$2 \cdot 10^6$ (at 7 T)
Nb_3Sn	18.3	23	$2 \cdot 10^4$ (at 20 T)

The first HTS conductor was discovered in 1986, and many have been discovered since [2]. In particular, cuprate superconductors with the rare-earth barium copper oxide (REBCO) composition exhibit high transition temperatures and good current density compared to LTS conductors [3]. HTS hold promise for future applications, due to the ability to operate magnets at higher temperatures and use liquid nitrogen as a cryogen. However, several remaining technical challenges currently limit the widespread use of HTS conductors. REBCO conductors are manufactured as thin tapes rather than round strands, the typical geometry for LTS conductors (Nb_3Sn and NbTi). It is challenging to develop cable configurations from the tape geometry with high current densities at high magnetic fields and under large loading conditions. Given the current state of

HTS research, LTS conductors such as Nb_3Sn and NbTi have remained the predominant materials used in high-field magnets.

1.3 Superconductor Applications

The primary use of commercially produced superconductors such as Nb_3Sn is in electromagnets for high magnetic field applications. These applications include nuclear fusion reactors, nuclear resonance imaging, and particle accelerators for high energy physics and proton therapy. Superconducting magnets consist of cylindrical coils, which are wound from cables. Cables are made up of multiple superconducting strands that are assembled in specific configurations that are dependent on the intended application and the type of superconductor. Other applications such as superconducting magnetic refrigeration, superconducting magnet energy storage, and superconducting power transmission are in earlier stages of research and development.

1.3.1 Nuclear Fusion Reactors

A nuclear fusion reactor is a proposed power generating facility that uses the fusion reaction of two hydrogen isotopes, commonly deuterium and tritium, to produce helium and energy. In order for this reaction to occur, the hydrogen nuclei must be brought to a high temperature and pressure, creating a plasma. The plasma is confined and controlled within the reactor using high magnetic fields produced by superconducting magnets.

The International Thermonuclear Experimental Reactor (ITER) is the largest fusion reactor project in the world, and is currently under development in France under the collaboration of seven different nations. The goal of the project is to demonstrate the feasibility of nuclear fusion power by producing steady-state, self-sustaining plasma using a tokamak design [4]. The multistage cables used in magnets for fusion reactors are called cable-in-conduit conductors (CICCs), which are made up of approximately 1000 Cu and superconducting (Nb_3Sn or NbTi) strands. It is estimated that ITER will use approximately 600 metric tons of Cr-plated Nb_3Sn and 275 metric tons of Ni-plated NbTi by the time it is completed [3], [4]. ITER has been the largest single use of Nb_3Sn strands in history, requiring significantly increased production to meet the needs of the project. Production has risen from approximately 15 metric tons/year before the development of ITER, to over 400 metric tons/year in 2013 [4]. Increased production and subsequent cost reductions from ITER provide benefits to other magnet applications that utilize Nb_3Sn materials, such as medical imaging and proton therapy.

1.3.2 Nuclear Magnetic Resonance Spectroscopy

Superconducting magnets are also components of nuclear magnetic resonance (NMR) spectrometers, which are used to identify the structure and properties of molecules for a variety of scientific applications. In a uniform magnetic field, different types of molecules absorb electromagnetic radiation at unique resonant frequencies. NMR machines identify the chemical composition of

substances by analyzing the spectrum of absorbed electromagnetic radiation. Superconducting magnets are used to produce the high magnetic fields required for this application. NMR spectrometers that operate at 1.5 K, 1 GHz, and 23.5 T and utilize magnets with coils of both Nb_3Sn and NbTi are now on the market. These magnet coils can operate continuously for years with minimal resistive losses after a current is initially applied by the manufacturer [3].

Magnetic resonance imaging (MRI) is a specific type of NMR that has become extremely important in the healthcare sector. MRI machines provide three dimensional imaging of the body by identifying the concentration of hydrogen atoms in different regions. Since each type of tissue is made up of different concentrations of hydrogen atoms (a component of water molecules), MRI can identify the precise location of different tissues. These detailed images of the body aid in medical diagnosis and analysis of different diseases. MRI machines generally use NbTi magnets with fields of 3 T or lower [3].

1.3.3 Particle Accelerators and Proton Therapy

Superconducting magnets are used to accelerate, focus, and bend particle beams in particle accelerators for high-energy physics experiments and medical applications. These magnets generally utilize the Rutherford cable design, in which individual strands are twisted to form a rectangular cross-section. Currently, NbTi is used almost exclusively in these magnets. However, to reach higher particle energy levels, future particle accelerators will need magnetic fields

greater than 9 T, requiring the use of Nb_3Sn or HTS conductors in magnets. Dipole and quadrupole Nb_3Sn magnets are scheduled to be installed over the next 10 years in the Large Hadron Collider, the most powerful particle accelerator in the world [5]. Challenges for the development of Nb_3Sn accelerator magnets are the brittle behavior of the material, stresses in the strand resulting from heat treatment, and the low ultimate strength relative to NbTi [3].

The cyclotron is a type of particle accelerator in which particles are accelerated in a planar spiral path. The particles bend due to Lorentz forces in the radial direction, resulting from a constant magnetic field applied normal to the acceleration plane. An RF electric field of constant frequency is applied between electrodes in the acceleration plane which causes particles to accelerate each time they pass. The orbital radius and energy level of the particles increase as they are accelerated. The particles are extracted through the rim of the vacuum sealed chamber into a beamline.

However, a loss of synchronism in the particle orbit is observed in cyclotrons for particle energy levels over 20 MeV. This occurs because the mass of the particle increases at higher energy levels due to relativistic effects, which lowers the orbital frequency and causes the particles to become out of phase with the electric field [6]. This problem was solved with the invention of the synchrocyclotron by Vladimir Veksler and Edwin McMillan in 1944 [7]. In a synchrocyclotron, the frequency of the RF electric field is decreased as the orbital radius of the particle increases, instead of being held constant. The modulation of

the frequency accounts for relativistic effects, improves the stability of the orbit, and allows particles to reach higher energy levels.

The superconducting synchrocyclotron was patented by Blosser et al. in 1987 [8]. The use of superconducting magnets rather than conventional magnets allows for higher magnetic fields, smaller acceleration radii, and lighter, more compact systems [9].

Mevion Medical Systems has developed a compact, single-room superconducting synchrocyclotron system for proton therapy that is currently being used by hospitals and cancer treatment facilities [1]. The Mevion S250 series achieved FDA clearance in 2012. The proton accelerator is gantry mounted and uses a magnetic field of 10 T and a bending radius of 0.3 m [10], producing a particle energy level of 250 MeV [9]. The superconducting cables used by Mevion consist of four Nb_3Sn strands twisted helically around a copper center wire.

Proton therapy provides unique advantages over other types of radiotherapy for cancer treatment, such as x-ray therapy. Proton therapy and x-ray therapy provide different distributions of radiation concentration at different tissue depths. Ideally, a treatment system should deliver radiation only at the depth of the tumor. However, x-ray treatment frequently leads to excess radiation at depths shallower than the tumor, leading to the overexposure of healthy tissue [9]. In proton therapy, the radiation dose is highly concentrated at the Bragg peak of the particle, which is dependent on the particle energy level and therefore can be tailored to match the depth of the tumor. A disadvantage of proton therapy

relative to x-ray systems is the high capital cost. However, the development of more compact systems may result in cost reductions.

1.4 Nb_3Sn Superconductors

1.4.1 Structure and Manufacturing

The superconducting properties of Nb_3Sn were discovered in 1954 by Matthias et al. [11]. Nb_3Sn belongs to a group of A15 superconductors, which have a type A_3B chemical composition, a simple cubic crystal structure, and Type II magnetic properties. V_3Ga and Nb_3Al are other A15 superconductors that may hold the promise for future commercial use.

Nb_3Sn is manufactured in the form of round strands, typically with a diameter of ~1 mm, which consist of thousands of superconducting filaments in a copper matrix. Each filament has a diameter of a few micrometers. The four most common manufacturing methods currently used to produce these strands are: (1) the bronze process, (2) the internal tin method, (3) the jelly roll method, and (4) the powder-in-tube method. These manufacturing processes are described briefly below and are discussed in greater detail in [3] and [5].

In the bronze process, Nb filaments are inserted into a bronze (Cu-Sn) cylinder to form a composite billet. The billet is extruded and bundled with other wires to create a wire of larger diameter. This wire is then rolled and drawn to the required dimensions and heat treated. The internal tin method is similar to the bronze method, except that the Nb filaments are inserted into a copper cylinder

with a tin core that diffuses into the composite billet during the heat treatment process (Figure 2a). The bundled elements are lined with a copper stabilizer and a tantalum diffusion barrier. In the jelly roll process, thin Nb and bronze foils are rolled around a copper rod with a tantalum diffusion barrier and then inserted into a copper tube. Many of these tubes are bundled together to create a composite billet, which is extruded and heat treated. In the powder-in-tube process, Nb tubes are placed in a copper matrix and filled with Nb_3Sn powder, and then heat treated (Figure 2b). The Nb_3Sn strands used in the ITER magnets are all manufactured using either the bronze or internal tin processes [4].

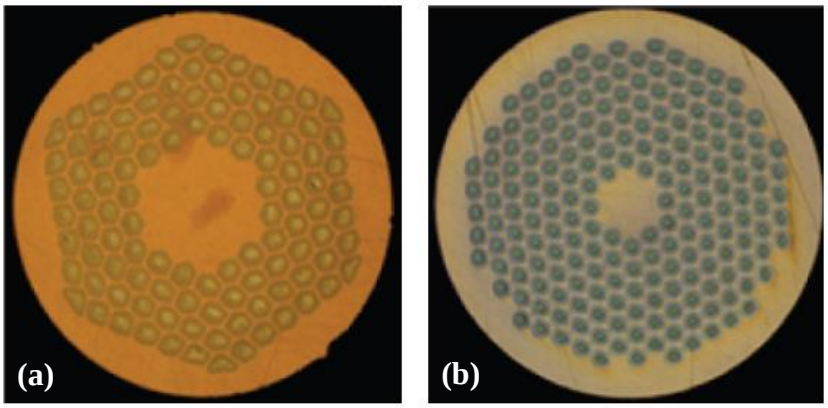

Figure 2: Cross-section of Nb_3Sn strands manufactured with the (a) internal tin and (b) powder-in-tube processes [5].

Strands are heat treated for several days at 650-750°C, during which Sn diffuses to the surface of the Nb filaments to form a superconducting layer of Nb_3Sn. The specific duration and temperature of heat treatment can vary depending on the manufacturing process [3], [5]. After heat treatment, the material becomes extremely brittle, limiting the mechanical performance of the strand. High stresses may fracture the brittle Nb filaments, damaging the electrical

properties of the strand. Stresses that exceed the fracture strength of the material may result in fracture of the entire strand. Because the material is still relatively ductile before heat treatment, cables are generally manufactured using a "wind-and-react" technique rather than a "react-and-wind" processes, especially if magnet coils with small radii are required.

1.4.2 Effect of Strain on Magnet Performance

As described in Section 1.2, the critical current density (J_c), critical magnetic field (B_c), and critical temperature (T_c) of a superconductor are interdependent and define the limits of the superconducting state of the material. Increasing the current, magnetic field, or temperature will reduce the other critical parameters. The critical current of Nb_3Sn also depends on strain. Various studies have empirically characterized the dependence of the critical current on strain and magnetic field for single strands [12], sub-cables, and CICCs [13]. Strands experience large loading conditions during magnet operation, including axial forces, transverse loads, and bending forces. Axial forces are experienced during the cooling process after heat treatment due to differences in the thermal contraction of different components of the strand. Bending and transverse loads are experienced during the cabling process and during magnet operation due to electromagnetic forces. Under these different loading conditions, strands experience strains that result in reductions in the critical current.

1.4.3 Tensile Testing

Due to the brittle nature of reacted Nb_3Sn and the effect of strain on critical current, stress-strain data is required to optimize the mechanical and electrical performance of magnets. Tensile testing can be used to determine various mechanical properties, including the Young's modulus, strength at fracture, and yield strength. These properties are dependent on the heat treatment procedure, mechanical properties of the Nb_3Sn filaments, and the Nb_3Sn to Cu volume ratio in the strand [14]. Once the properties of individual strands are known, finite element analysis (FEA) can be used to evaluate the behavior of cables or magnets that are composed of many strands.

Tensile testing is a fundamental and well-established testing method used to determine the mechanical properties of various materials. However, reacted Nb_3Sn strands are very brittle and have small diameters, which prevents the use of typical tensile testing procedures and equipment, such as Instron machines. Sample grips must be designed to hold the sample securely in place but avoid applying stress concentrations that that may result in premature fracture during testing. The small diameter of the strands (~0.8 mm) prevents the use of typical "dog bone" shaped samples.

The International Electrotechnical Commission (IEC) has issued the only official standard that covers the tensile testing of reacted Nb_3Sn strands at room temperature. This draft, titled "Mechanical properties measurement – Room temperature tensile test of composite superconductors", is Part 6 of International Standard IEC 61788 [15]. Many of the guidelines in the standard are based on the

findings of an international round robin test performed by 11 research laboratories from around the world [16]. Throughout this study, the standard has been used to specify the appropriate procedures for testing and data processing, and is referred to hereafter as IEC Standard 61788-6. It should be noted that the standard was developed specifically for reacted Nb_3Sn strands, and therefore is not directly applicable to all of the samples that were tested in this study.

Numerous other studies have performed tensile tests on both reacted and unreacted Nb_3Sn strands at room temperature [14], [17]–[19]. The results from these studies give the mechanical properties of specific samples and show the effect of heat treatment on mechanical properties.

An official standard for the tensile testing of Nb_3Sn cables does not currently exist. However, twisted wire cables are used in a variety of non-superconducting applications. Standards such as ASTM A 931-96 and ASTM A 416 have been established to address the tensile testing of these cables. These documents provide qualitative guidance on the appropriate testing procedures for cable samples.

1.5 Thesis Scope

This thesis provides an overview of the tensile testing and analysis of the mechanical properties of Nb_3Sn strands and cables provided by Mevion Medical Systems. The experimental methods are described in Section 2, covering the specifications of the tensile testing apparatus and data acquisition system, design of the sample grips, experimental testing procedure, post-processing, statistical

treatment of the data, and uncertainty analysis of the instrumentation. In Section 3, the empirical results are presented and discussed, and potential sources of error are considered. Section 4 provides a brief literature review of the mechanical theory of wire ropes. The effective Young's modulus of the reacted Nb_3Sn cable is evaluated analytically and compared to the empirical results. The primary conclusions from this study and recommendations for improvements to the existing tensile testing apparatus are outlined in Section 5. Supplementary material, including the stress-strain curves of all samples and CAD drawings of the sample grips, are included in the appendices.

2. Experimental Methods

2.1 Test Samples

Preliminary tests were first performed on copper strands to verify the performance of the tensile testing apparatus and establish an appropriate experimental procedure. The average strand diameter was 0.803 mm, which was 0.022 mm larger than the average diameter of the reacted Nb_3Sn strands from Mevion. Prior to testing, the copper strands were slightly curved along the entire length, having been taken from a spool.

The quantities of the reacted and unreacted Nb_3Sn strands and cables from Mevion are listed in Table 2. As shown in Figure 3, the cables were slightly bent prior to testing. The reacted Nb_3Sn strands were relatively straight and were provided in quartz tubing for protection. The unreacted Nb_3Sn strands were initially wavy, bent, and twisted because they had been removed from a twisted cable. The effect of this initial strand configuration on the mechanical properties is discussed in Section 3.3.

Table 2: Nb_3Sn samples tested for Mevion Medical Systems.

Sample Type	Heat Treatment	Quantity	Grip-to-Grip Length (mm)	Sample Length (mm)	Average Strand Diameter (mm)
Strand	Reacted	6	45	65	0.781
Strand	Unreacted	4	100	120	0.766
Cable	Reacted	10	120	180	0.786
Cable	Unreacted	10	120	180	0.774

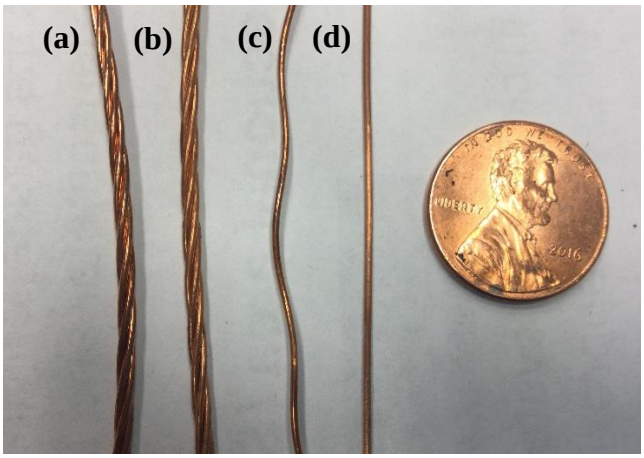

Figure 3: Nb_3Sn samples from Mevion: (a) unreacted cable, (b) reacted cable, (c) unreacted strand, and (d) reacted strand.

The cables consisted of four Nb_3Sn strands twisted around a copper center wire with a twist pitch of 20 mm. The twist pitch is the distance along the cable axis corresponding with one full revolution of a side strand. The cross-section of the reacted cable is shown in Figure 4 with the dimensions that were provided by Mevion. The actual diameters of the strands and cables deviated from these values, as shown in Table 2. The diameter of the reacted strands was larger than the diameter of the unreacted strands as a result of the heat treatment process, and all sample diameters were less than the nominal dimensions specified by Mevion.

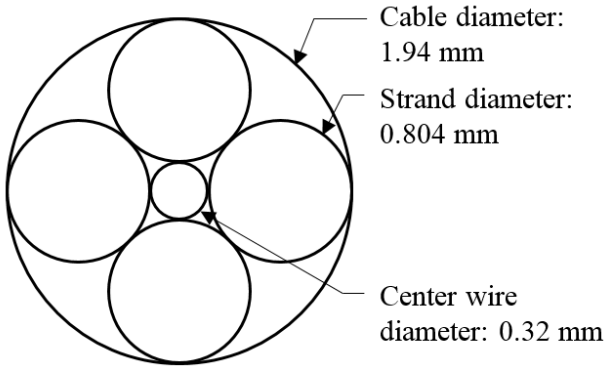

Figure 4: Cross-section of the reacted cable with dimensions specified by Mevion.

IEC Standard 61788-6 [15] recommends a minimum sample length of 60 mm for testing reacted Nb_3Sn strands. Since the procedure for testing REBCO tapes is very similar to the procedure for testing Nb_3Sn strands, the IEC standard for the tensile testing of REBCO tapes at cryogenic temperatures [20] was also considered. This standard advises that the minimum sample length (L_{sm}) should be equal to:

$$L_{sm} = 2L_g + L_{GL} + 2L_x \quad (1)$$

$$L_x = 0.7L_{GL} \quad (2)$$

where L_g is the grip length, L_{GL} is the gauge length of the extensometers used to measure the sample strain, and L_x is the distance between the sample grip and the extensometers. The position of the extensometers on the strand is shown in Figure *5* in the following section. The grip length L_g is the length of the portion of the sample that is gripped inside each of the sample holders. For the strand measurements, L_{GL} = 25 mm and L_g = 10 mm, resulting in a minimum sample length of 80 mm. To comply with both standards, a sample length of 120 mm was used for the unreacted strands. However, the provided reacted Nb_3Sn strands were 65 – 70 mm in length, which is less than the minimum sample lengths recommended by both standards. For consistency, all of the reacted strands were cut to a sample length of 65 mm length before testing. For the cable measurements, L_{GL} = 25 mm and L_g = 30 mm, resulting in a minimum sample length of 120 mm. The reacted and unreacted cables were tested with a sample length of 180 mm.

The grip-to-grip length and average strand diameter for each sample type are shown in Table 2. The grip-to-grip length is defined as the initial distance between the two sample grips, which is the length of the portion of the sample to which strain is applied during testing. For each test, the diameter of the strand was measured in five locations in two orthogonal directions using a micrometer, and the mean of all 10 measurements was calculated.

2.2 Tensile Testing Apparatus and Data Acquisition System

Tensile testing was performed using a tensile testing apparatus (Figure 5a) that was developed for similar experiments [21]. During testing, a constant vertical displacement was applied to the pull rod using a 10 kN Duff Norton machine screw linear actuator with a 20:1 gear ratio. An anti-backlash nut in the linear actuator reduced slack between the machine screw threads when the actuator motion was halted or reversed. A constant torque was applied to the linear actuator with a Bison 1/40 HP permanent magnet DC motor with a maximum torque of 100 in·lbf. The speed and direction of the motor was controlled during testing with a Minarik controller. A 250 lbf (1.1 kN) donut style load cell from Futek was used to measure the load applied to the sample. The load cell was mounted on the frame of the tensile testing apparatus such that it was in compression when a tensile load was applied. A linear variable differential transformer (LVDT) with a range of 15 mm was used to measure the displacement of the pull rod. The displacement of the strands was measured with Nyilas-type double extensometers with a gauge length of 25 mm. The

extensometers were mounted directly on the strands, as shown in Figure 5b. The weight of the extensometers was 2.8 g, which is well below the maximum extensometer weight recommended by IEC Standard 61788-6 of 30 g [15]. The design of the sample grips is discussed in Section 2.3. The main structural components of the tensile testing apparatus were made of 316 stainless steel and G10-FR fiberglass epoxy (shown in green in Figure 5).

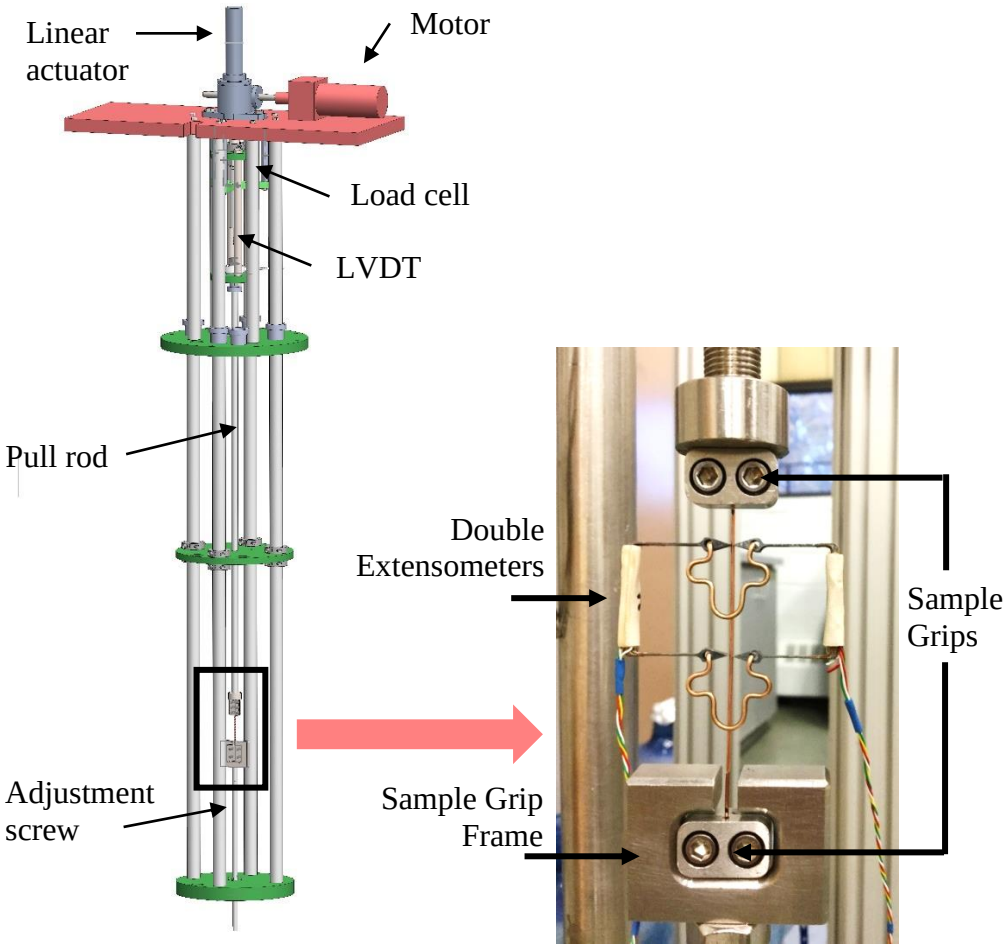

Figure 5: Overall model of tensile testing apparatus (left) and close up of sample area showing the extensometers mounted on a strand (right).

Four Keithley 2182A Nanovoltmeters were used to measure the voltage signals from the load cell, two extensometers, and LVDT. Power supplies were

used to provide excitation voltages to the sensors. A CEME four channel low noise signal conditioner with a Vishay Company BA 660 chipset was used to reduce noise in the measurements from the extensometers. Using a GPIB connection, data was recorded with a LabVIEW program designed by the National High Magnetic Field Laboratory.

2.3 Sample Grip Design

Sample grips were designed to keep the sample aligned in the axial direction, while applying a strain at a constant rate. IEC Standard 61788-6 recommends two different gripping methods which are shown in Figure 6 [15]. In the first design shown on the left, a strand is soldered to the inside of a brass thread which is fixed to an aluminum sleeve. When a load is applied to the sample, the sleeve makes contact with a metal frame, fixing the end of the sample in place. In the second design shown on the right, a strand is clamped between two aluminum plates in a v-shaped groove. The clamped aluminum plates sit inside an aluminum frame, and become fixed when the frame and plates come into contact as a load is applied to the sample.

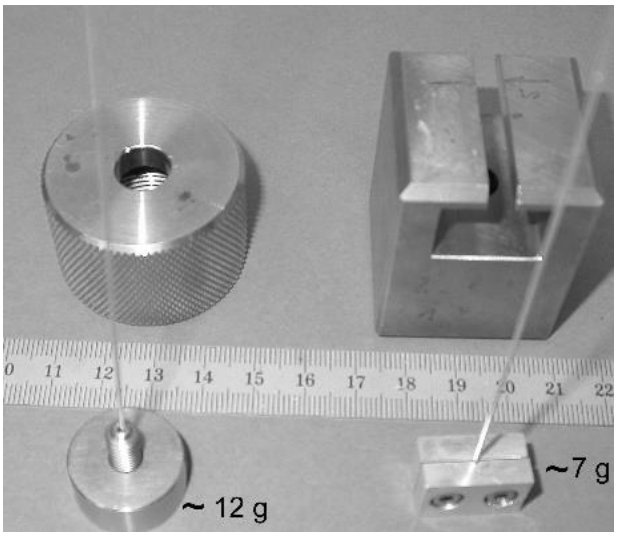

Figure 6: Sample gripping methods recommended by IEC Standard 61788-6 for the tensile testing of reacted Nb_3Sn strands [15].

Past studies have utilized a variety of different sample grip designs for testing Nb_3Sn strands. Several round robin testing laboratories have used methods similar to the two designs recommended by IEC Standard 61788-6 [16]. Standard precision drill chucks have also been used in various studies [16], [18].

For this study, a variation of the flat plate v-groove gripping method was used, primarily due to the ease of fabrication and the compatibility of the design with the existing tensile testing apparatus. The top sample grip is fixed to the pull rod and the frame of the bottom sample grip is attached to the bottom plate of the apparatus with a threaded rod. The bottom sample grip is initially hangs freely inside the bottom sample grip frame. When a load is applied to the sample, the bottom sample grip makes contact with the bottom sample grip frame and becomes fixed.

Existing sample grips that were originally fabricated for similar tests [21] were used for testing the strands (Figure 7). The flat plates were made of 316 stainless steel and were clamped together using 8-36 316 stainless steel socket

head cap screws. The grip length of the sample grips was 10 mm. The original depth of the v-groove was reduced from 0.381 mm (0.015 in) to 0.356 mm (0.014 in), based on the diameter of the Mevion strands. The optimal depth was determined from observations of past experiments [21], which suggested that a groove depth to diameter ratio of 0.47 was optimal to prevent slippage of the sample.

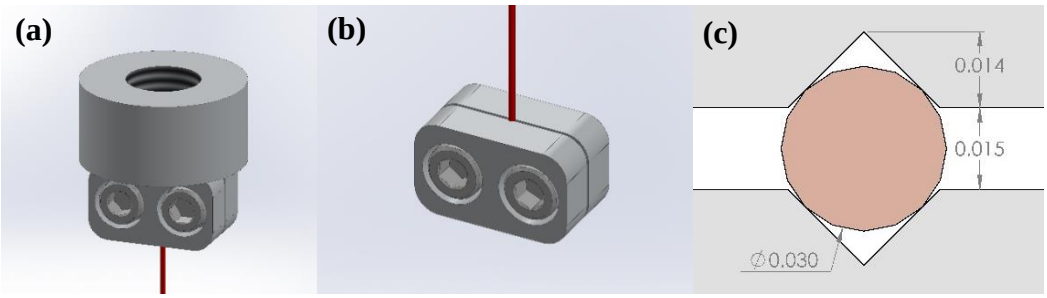

Figure 7: Design of the sample grips used for strand measurements: (a) top sample grip, (b) bottom sample grip, and (c) v-groove cross-section of the sample grips. Units are in inches.

Additional sample grips with a similar design were fabricated for the cable measurements. SolidWorks CAD drawings of the assembled grips are shown in Figure 8, and the complete part drawings are included in Appendix A. The plates were made from 304 stainless steel and clamped together and mounted on the tensile testing apparatus in the same manner as the sample grips for the strand measurements. The depth of the v-groove was sized to the cable dimensions provided by Mevion, using the same groove depth to diameter ratio recommended by previous work (0.47) [21]. The sample grips were designed with a grip length (30 mm) that was 50% larger than the twist pitch of the cable (20 mm) to ensure sufficient contact between the individual cable strands and the v-groove.

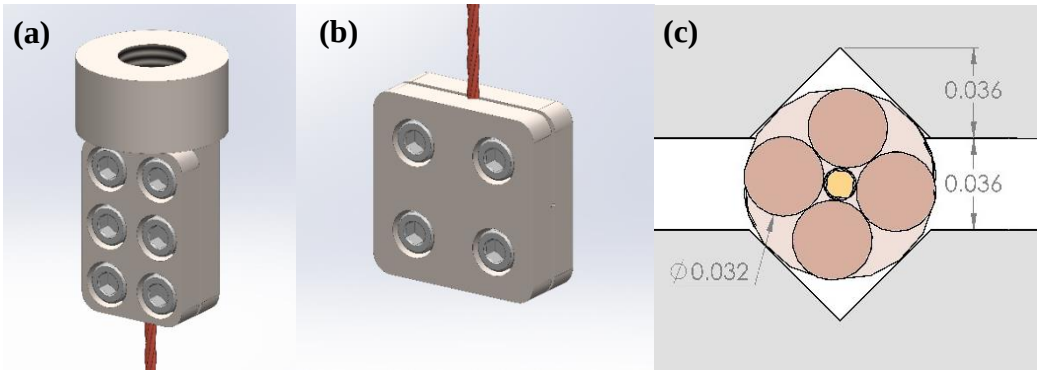

Figure 8: Design of the sample grips for the cable measurements: (a) top sample grip, (b) bottom sample grip, and (c) cross-section of the cable and v-groove. Units are in inches.

2.4 Experimental Procedure

The following testing procedure was determined from IEC Standard 61788-6 [15] and observations from preliminary tests on the copper strands.

The sample was mounted in the bottom sample grip by clamping the sample between the two gripping plates with the end aligned with the end of the sample grip. In order to provide uniform compression across the entire grip length, a specific torque was applied incrementally to each screw using a torque wrench. The appropriate torque to apply to the sample grip screw for each sample type was determined through trial and error. When the applied torque was too low, the sample slipped in the sample grip. When the applied torque was too high, stress concentrations resulted in premature fracture of the sample at the sample grips. It is generally accepted that the results of tensile tests are valid only if fracture occurs in the middle of the sample, rather than at the edge of or inside the sample grips [22]. This only happens if the stress concentrations at the sample grips are sufficiently low. The optimal torques were found to be 1.36 N·m (12

in·lbf) for the unreacted strands, 0.56 N·m (5 in·lbf) for the reacted strands, 0.34 N·m (3 in·lbf) for the reacted cables, and 1.13 N·m (10 in·lbf) and 2.60 N·m (23 in·lbf) for the unreacted cables for the top and bottom sample grips respectively. A lower torque must be applied to the reacted samples because they are brittle and more susceptible to premature fracture.

The sample was mounted in the top sample grip in a similar manner. The top sample grip was attached to the pull rod prior to mounting to avoid applying torsion to the sample. The sample was mounted such that the bottom sample grip was hanging freely in the frame to avoid applying any axial strain prior to testing.

Slippage of the sample in the sample grip v-groove occurred during preliminary tests on copper strands. Various techniques were used to attempt to mitigate this problem before testing the samples provided by Mevion. Roughening the surface of the copper strands with sandpaper along the grip length resulted in slippage at an even lower level of strain, likely due to the slight reduction in the sample diameter. Increasing the torque applied to the screws of the sample grip increased the load at which slipping occurred, but only up to a certain level. The use of sandpaper between the sample grips was the most effective, resulting in an increase in the maximum attainable applied load by 42.5%. Therefore, a double layer of sandpaper was placed on either side of the strand or cable when testing the Nb_3Sn samples, as shown in Figure 9.

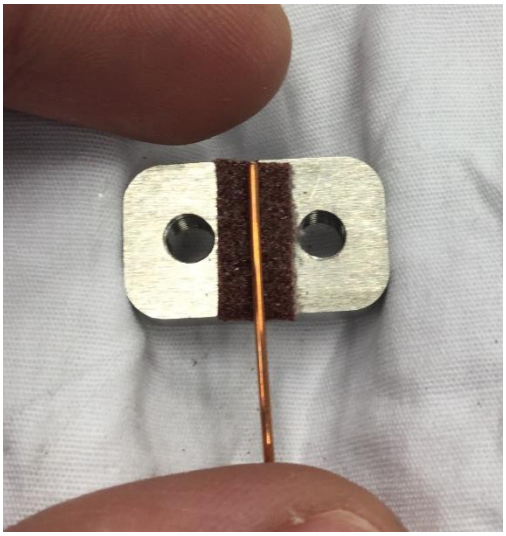

Figure 9: Placement of sandpaper in the lower sample grip for strand measurements.

For the strand measurements, the extensometers were mounted on the middle of the sample as shown in Figure 5b. The extensometer tips were aligned as evenly as possible to avoid applying shear stress to the sample.

Strain was applied to the sample at a constant rate of 0.3 mm/min, or 46% of the maximum speed of the motor. This testing speed was chosen based on IEC Standard 61788-6, which recommends a constant testing speed between 0.1 and 0.5 mm/min [15]. IEC Standard 61788-6 suggests unloading the sample at 0.3-0.4% strain by 30-40% of the load [15]. However due to a problem with the tensile testing apparatus that is discussed in Section 3.1, some samples were unloaded by up to 50% of the applied load. At the point of unloading, the motor was stopped and run in reverse at the same testing speed. After unloading, the sample was reloaded until the sample either fractured or slipped inside the sample grip.

2.5 Data Post-Processing

2.5.1 Calculation of Stress and Strain

The raw voltage signals from the LVDT, extensometers, and load cell were converted to values of displacement and applied load by multiplying by the sensitivity of each sensor. The sensitivities were 1112 N/20 mV for the load cell and 15 mm/10 V for the LVDT. The extensometers were calibrated before the first experiment and again approximately half-way through the experiments. For each calibration, the extensometers were mounted on a micrometer with a flat-faced anvil and spindle and the displacement of the spindle was increased from 0 to 2.4 mm (working range of the extensometers) in 0.2 mm increments. The voltage output was recorded at each level of displacement, and the sensitivity was obtained from slope of the displacement-voltage graph using linear regression. The average sensitivities for the two extensometers were 1.821 mm/V and 1.736 mm/V with less than 3% deviation between the two calibrations.

Stress and strain were calculated from the displacement and applied load. Strain is a measure of the deformation of a material, and is defined as an incremental change in length divided by the initial length:

$$\varepsilon = \frac{\Delta l}{l} \tag{3}$$

Stress is defined as the magnitude of an applied load divided by the cross-sectional area of the material, as shown in Equation 4. Stress is typically expressed in units of Pascals (Pa), which are equal to one Newton (N) per square meter.

$$\sigma = \frac{F}{A} \quad (4)$$

There are two definitions of stress: engineering stress and true stress. The difference arises due to alternate definitions of the cross-sectional area in the denominator of Equation 4. When a tensile load is applied to a sample in the axial direction, the material exhibits tensile strain in the axial direction and compressive strain in the transverse direction, due to the Poisson effect. This causes the cross-sectional area of the sample to become smaller as axial strain is applied. The cross-sectional area may also decrease due to necking, which is the localized yielding that occurs in many metallic materials just prior to fracture during plastic deformation. The engineering stress is calculated using the initial cross-sectional area of the sample, while the true stress is calculated using the instantaneous cross-sectional area. Measurement of true stress is more difficult than measurement of engineering stress because it requires measurement of the sample area over time, which involves more complex instrumentation. Therefore, most studies measure engineering stress rather than true stress. All further discussion of stress in this study refers to engineering stress.

2.5.2 LVDT Calibration

During testing, the displacement of the pull rod differed from the displacement of the sample itself due to compliance of the tensile testing apparatus. The LVDT measures the displacement of the pull rod, and extensometers measure the displacement of the sample. Therefore, it is more

accurate to use the measurements from the extensometers to calculate the sample strain. However, the extensometers cannot be mounted on the cable due to the non-uniform cross-section along the length of the cable and the difference between the twist pitch of the cable (20 mm) and the gauge length of the extensometers (25 mm). Therefore, the measurements from the LVDT were used to calculate the strain for the cable tests, using a unitless bias factor to account for the compliance of the tensile testing apparatus.

The bias factor was determined by calibrating the sensitivity of the LVDT with the sensitivity of the extensometers. The average bias factor for the copper strands was 0.648 and the standard deviation was 0.061. For the reacted Nb_3Sn strands, the average bias factor was 0.621 and the standard deviation was 0.011. The LVDT was not calibrated for the unreacted Nb_3Sn strands because valid material property data was not obtained, as discussed in Section 3.3. Therefore the bias factor for copper was used to calibrate the LVDT for the unreacted cables. It was assumed that the bias factor is not dependent on the cross sectional area or length of the sample.

2.5.3 Calculation of Mechanical Properties

The Young's modulus (E) or modulus of elasticity is a measure of the stiffness of a material. It is defined as the tensile stress in the axial direction (σ)

divided by the strain in the axial direction (ε), or the slope of the stress-strain curve in the linear elastic region:

$$E = \frac{\sigma}{\varepsilon} \tag{5}$$

For a strand, the application of a tensile load in the axial direction results in both axial and transverse strain. The application of a tensile load to a cable also results in bending strain, due to the twisted configuration of the strands. Therefore, the interpretation of the Young's modulus is somewhat different when applied to a cable, since Equation 5 does not strictly apply. The Young's modulus of a cable can be considered to be a measure of the overall stiffness of the cable, rather than the stiffness of the material itself.

The Young's modulus was evaluated for the initial loading (E_o) and the unloading of the sample (E_u). The process for determining the linear elastic region was automated to avoid introducing any bias into the calculations. A linear regression was performed on the initial region of the stress-strain curve, while iteratively increasing the maximum bound of the region. The region that resulted in the largest coefficient of determination (R^2 value) from the regression was selected as the linear elastic region.

IEC Standard 61788-6 recommends that E_u should be calculated from the slope of the portion of the unloading curve corresponding to 99% and 90% of the applied load at the point of unloading [15]. However, the stress-strain curves obtained from these experiments lacked a sharp transition from the loading curve to the unloading curve, which made it impossible to follow these guidelines.

Instead E_u was calculated based on the entire portion of the unloading stress-strain curve.

Theoretically, E_o and E_u should be equal for a single strand, although they tend to vary in practice. Potential reasons for this variation are discussed in Section 3.6. IEC Standard 61788-6 provides the following equation for checking the validity of test results [15]:

$$1 - \Delta < \frac{E_o}{E_u} < 1 + \Delta \tag{6}$$

The results are considered valid when Equation 6 holds true for $\Delta = 0.3$. The international round robin test concluded that setting $\Delta = 0.3$ reduces the coefficient of variation to a statistically acceptable level [16]. The actual deviation between E_o and E_u for a specific sample can be calculated from Equation 7, where $\Delta_a = 0$ when E_o and E_u are equal.

$$\Delta_a = \left|1 - \frac{E_0}{E_u}\right| \tag{7}$$

The yield stress ($S_{Y0.2\%}$) was calculated using the 0.2% offset method. A line was drawn on the stress-strain plot with a slope equal to E_o and an x-intercept of $\varepsilon = 0.2\%$. $S_{Y0.2\%}$ was defined as the level of stress associated with the point of intersection between the line and the stress-strain curve.

The fracture strength (S_u) was calculated as the stress at the point on the stress-strain plot at which the sample fractured.

2.5.4 Uncertainty Analysis

An uncertainty analysis was performed to quantitatively assess the contributions of different experimental uncertainties to the variation in the empirical results. The elemental uncertainties associated with each measurement device were obtained from manufacturer specifications (Table 3). Each uncertainty was categorized as either a systematic or random uncertainty.

Table 3: Elemental systematic and random uncertainties of measurement devices obtained from manufacturer specifications.

Component	Measured variable	Type of uncertainty	Systematic/ random	Uncertainty (FSO = full scale output)
Load cell	Applied load	Zero balance	Systematic	±1% FSO
		Linearity	Systematic	±0.5% FSO
		Hysteresis	Systematic	±0.5% FSO
		Nonrepeatability	Random	±0.5% FSO
LVDT	Elongation (for cable tests)	Linearity	Systematic	±0.2% FSO
		Output ripple	Systematic	±0.02% FSO
Extensometers	Elongation (for strand tests)	Linearity	Systematic	±0.01% FSO
Voltmeter	Applied load and elongation	Linearity	Systematic	± (0.8 ppm reading + 0.5 ppm FSO)
Micrometer	Sample diameter	"Accuracy"	Systematic	±0.001 mm

The elemental systematic and random uncertainties of the measurement equipment (B_i and P_i) were used to estimate the systematic and random uncertainties associated with each measured variable (B_x and P_x). For example, the elemental uncertainties for the zero balance, linearity, hysteresis, and nonrepeatability of the load cell and linearity of the voltmeter were used to calculate the systematic and random uncertainties of the applied load. In order to give a conservative estimate of uncertainty that is applicable to all measurements, the linearity error of the voltmeter was expressed as a fraction of the full scale output (FSO) rather than the actual reading.

$$B_x = \left[\sum_{i=1}^{k} {B_i}^2\right]^{\frac{1}{2}} \qquad S_x = \left[\sum_{i=1}^{m} {S_i}^2\right]^{\frac{1}{2}} \qquad P_x = \frac{tS_x}{\sqrt{M}} \tag{8}$$

The random uncertainty in a measured variable (P_x) can be calculated from the standard deviation of the measured variable (S_x). It is assumed that all elemental uncertainties represent a 95% level of confidence. The overall uncertainty of a single measurement of a measured variable (W_x) was calculated from the systematic and random uncertainties:

$$W_x = \left({B_x}^2 + {P_x}^2\right)^{\frac{1}{2}} \tag{9}$$

The overall uncertainties were calculated to be ±14.71 N for the applied load, ±0.001 mm for the sample diameter, ±0.0025 mm for the displacement measured by the extensometers (±0.010% strain), and ±0.0301 mm for the displacement measured by the LVDT (0.067% strain for a 45 mm grip-to-grip length, 0.025% strain for 120 mm grip-to-grip length). Therefore, the extensometers had a lower uncertainty than the LVDT for strain measurement. When using the LVDT, the use of a longer grip-to-grip length resulted in lower uncertainty.

The uncertainty analysis did not account for any potential bias that was introduced from the manual determination of the offset. Any bias that was introduced through this process may have affected the calculation of E_o, although it is difficult to express this potential error quantitatively. In the future, the determination of the initial point of loading should be automated to eliminate any bias.

The uncertainties calculated in this analysis are attributed to the measurement equipment, rather than the statistical variation of the mechanical properties of the samples. In contrast, the variation in the results in Section 3 represents both the uncertainty of the instrumentation and the statistical variation of the material properties. In the following analysis, the mean, standard deviation, and coefficient of variation of each material property (E_o, E_u, $S_{Y0.2\%}$, S_u) were evaluated for each sample type. The mean and standard deviation of the stress were calculated as a function of strain, and displayed as a stress-strain plot (mean) with error bars (standard deviation).

3. Experimental Results and Discussion

Table 4 shows the quantity, average diameter, and mechanical properties that were calculated for each different type of sample. The reason why each test was terminated, such as sample slippage, fracture, or reaching the maximum capacity of the equipment, is also listed. The results for each sample type are discussed in the following sections.

Table 4: Characteristics of tested samples and calculated properties and notes on testing and sample fracture for each sample type.

Sample type	Quantity	Avg. strand diameter (mm)	Calculated properties	Reason for test termination
Cu strand	11	0.803	E_o, E_u, $S_{Y0.2\%}$	Sample slippage or fracture at sample grip
Nb_3Sn reacted strand	6	0.781	E_o, E_u, S_u	Fracture in middle of sample or at sample grip
Nb_3Sn unreacted strand	4	0.766	-	Sample slippage or fracture at sample grip
Nb_3Sn reacted cable	10	0.786	E_o, E_u	Sample slippage or fracture at sample grip
Nb_3Sn unreacted cable	10	0.774	E_o, E_u, $S_{Y0.2\%}$	Sample slippage or reached maximum load cell capacity

3.1. Reference Material: Copper Strand

Eleven copper strands were tested, and the mean, standard deviation, and coefficient of variation for E_o, E_u, and $S_{Y0.2\%}$ are shown in

Table *5*. The values for E_o were calculated from the results of all 11 tests, and the values for E_u were calculated from the results of the four tests in which the strand was unloaded. The values for $S_{Y0.2\%}$ were calculated from 10 of the tests, because one of the tests did not reach a high enough strain to perform the calculations. All

tests ultimately resulted in slippage of the strand within the sample grip or premature fracture at the edge of the sample grip. Therefore, the strength at fracture (S_u) was not reported.

The value of E_o for a copper alloy is around 110 GPa, although it may vary widely depending on the specific alloy composition [23]. Therefore, the mean measured value of E_o = 119.2 GPa is within the range of expected values. The yield strength of a copper alloy can vary by up to an order of magnitude depending on the alloy composition. Previous measurements of a similar copper alloys found yield strengths between 375 and 388 GPa [21], which is reasonably similar to the results shown in Table 5.

The low coefficients of variation for E_o (4.2%) and $S_{Y0.2\%}$ (3.6%) show good consistency between tests. The larger coefficient of variation for E_u may be attributable to the small number of samples for which E_u was calculated. Additionally, these tests were not all performed with the same testing procedure (i.e. sample grip compression, testing speed, grip-to-grip length, sample mounting), since the purpose of these measurements were to identify an appropriate methodology. This may have caused some variation in the results.

Table 5**:** Mean, standard deviation, and coefficient of variation of E_o, E_u, and $S_{Y0.2\%}$ for the copper strands.

	Mean	Standard deviation	Coefficient of variation
E_o [GPa]	119.2	5.0	0.042
E_u [GPa]	177.4	29.8	0.168
$S_{Y0.2\%}$ [MPa]	399.8	14.5	0.036

The mean and standard deviation of the stress as a function of strain are shown in Figure 10. The standard deviation was calculated up to the smallest value of the maximum strain for all tests to maintain a constant sample size (N=11). The maximum standard deviation was 14.95 MPa. Note that the standard deviation is small for low values of strain because the stress-strain curves were zeroed at the origin during post-processing.

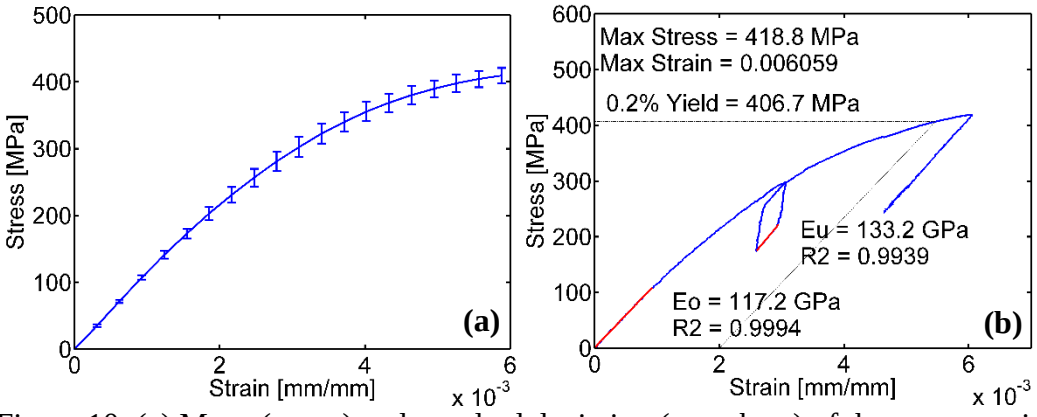

Figure 10: (a) Mean (curve) and standard deviation (error bars) of the stress-strain curves for the copper strands and (b) a stress-strain curve for sample #11.

One of the individual stress-strain curves (sample #11) shown in Figure 10b illustrates an issue with the tensile testing apparatus that was discovered while testing the copper strands. From basic knowledge of the mechanics of metals, the initial loading, unloading, and reloading stress-strain curves should have similar slopes. For some materials, there is an offset between the unloading and reloading stress-strain curves due to hysteresis. Copper and Nb_3Sn do not generally show much hysteresis. However, the stress-strain curves for the copper strands showed a large offset between the unloading and reload curves due to a rapid decrease in the load cell signal at the point of unloading (see Figure 10b at

approximately 0.3% strain). The magnitude of the drop in the load was relatively consistent between different tests, ranging from 34.1 to 42.4 N.

It was determined that the drop in the load at the point of unloading was not due to hysteresis, but slack in the apparatus due to how the LVDT was mounted. Figure 11 shows the stress-strain curves of a copper strand under two test conditions: when the LVDT was operating normally (green) and when the LVDT was disabled (blue). By disabling the LVDT, the drop in the applied load at the point of unloading was reduced by 88.5% (from 41.3 N to 4.7 N). The small remaining slack may be attributable to backlash in the motor or linear actuator. Although disabling the LVDT did reduce the slack in the apparatus, the LVDT was needed to measure the strain for the cable measurements and could not be disabled during the tests. Recommended improvements to the tensile testing apparatus, including the LVDT, are made in Section 5.2.

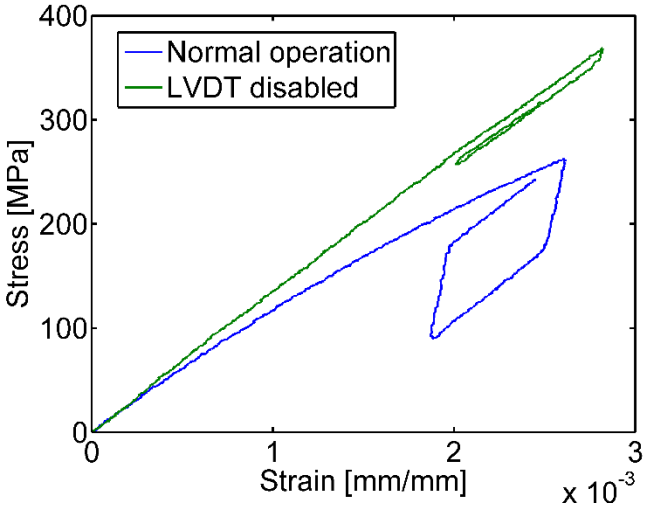

Figure 11: Stress-strain curve of a copper strand, showing the effect of slack in the tensile testing apparatus at the point of unloading.

Due to the lack of a sharp transition between the loading and unloading curves, E_u could not be calculated from the portion of the unloading curve corresponding with 99% to 90% of the applied load at the point of unloading. Instead, E_u was measured from the entire portion of the unloading curve after the initial drop in the load cell signal. Although the slack in the apparatus did not seem to affect the slope of the unloading curve or the magnitude of E_u, it limited the portion of the unloading curve that could be analyzed when the sample was only unloaded by 30-40% of the applied load. Therefore, some of the Mevion samples were unloaded by up to 50% of the applied load to measure a larger portion of the unloading curve.

3.2 Reacted Nb_3Sn Strands

Measurements were performed on six reacted Nb_3Sn strands, and the results for E_o, E_u, and S_u for each strand are shown in Table 6. Four of the strands fractured at the sample grips (#1, 2, 3 and 5) and two fractured in the middle of the strand (#4 and 6). Fracture in the middle of the strand confirms the validity of the S_u measurements. Premature fracture generally occurs at the sample grips due to stress concentrations. Three of the strands were not unloaded because fracture occurred before 0.3% strain. None of the strands reached a high enough strain to calculate $S_{Y0.2\%}$ using the 0.2% offset method.

Δ_a was calculated for the three strands that were unloaded, and only one strand violated Equation 6 such that $\Delta_a > 0.3$. The international round robin test omitted results for samples where $\Delta_a > 0.3$ to reduce scatter. Since only some

strands were unloaded and Δ_a could only be evaluated for those strands, results were not omitted on this basis to avoid introducing bias.

Table 6: E_o, E_u, and S_u for each reacted Nb_3Sn strand.

Sample	#1	#2	#3	#4	#5	#6
E_o [GPa]	72.25	95.40	98.44	99.73	108.92	86.36
E_u [GPa]	135.17	--	--	119.28	--	115.68
S_u [MPa]	266.15	185.41	191.79	256.60	237.08	250.79

The mean, standard deviation and coefficient of variation of E_o, E_u, and S_u for the reacted strands are shown in Table 7. The values for E_o and S_u were calculated from the results of all six tests, and the values for E_u were calculated from the results of the three tests in which the strands were unloaded (#1, 4 and 6). The values in parenthesis for S_u were calculated from the results of the tests in which the strand fractured in the middle. The coefficient of variation for S_u was high (14.9%) when the results of all tests were considered, due to the variability associated with the premature fracture of some strands. The coefficient of variation decreased to 1.6% when only the results of the tests that resulted in fracture in the middle of the strand were considered.

The international round robin performed tests on reacted Nb_3Sn strands from Hitachi with a diameter similar to those provided by Mevion (d = 0.80 mm) [16]. These materials should be expected to have properties that are similar but not identical to the properties of the reacted Nb_3Sn strands from Mevion. As anticipated, the mean values of E_o, E_u, and S_u of the two types of strands were within 10% of each other.

Table 7: Mean, standard deviation, and coefficient of variation of E_o, E_u, and S_u for the reacted Nb_3Sn strands.

	Mean	Standard deviation	Coefficient of variation
E_o [GPa]	93.5	12.7	0.136
E_u [GPa]	123.4	10.4	0.084
S_u [MPa]	231.3 (253.7)	34.5 (4.1)	0.149 (0.016)

The mean and standard deviation of the stress as a function of strain for all six tests are shown in Figure 12a. The maximum standard deviation was 6.14 MPa. All samples exhibited stress-strain curves characteristic of reacted Nb_3Sn strands, namely a narrow linear elastic region extending to 0.02 - 0.03% strain followed by a linear plastic region that ultimately resulted in brittle fracture of the material. An example of a stress-strain curve for one of the reacted strands is shown in Figure 12b.

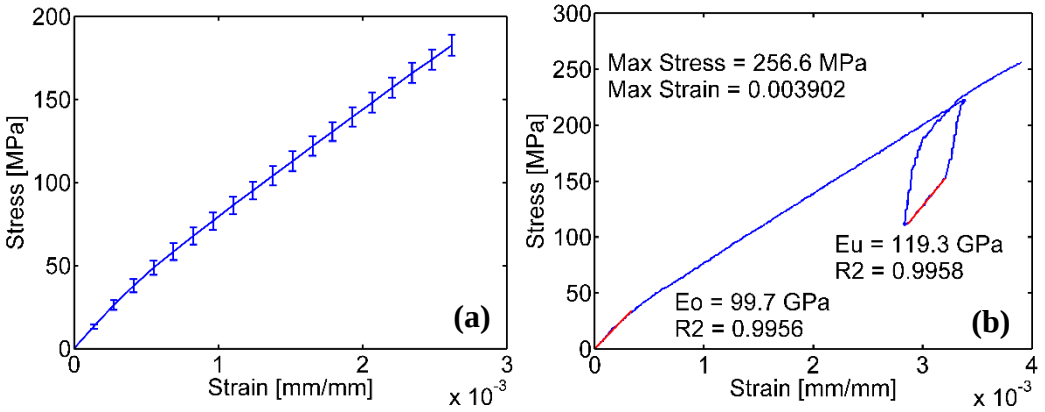

Figure 12: (a) Mean (curve) and standard deviation (error bars) of the stress-strain curves for the reacted Nb_3Sn strands and (b) a stress-strain curve for reacted Nb_3Sn strand #4.

3.3 Unreacted Nb_3Sn Strands

Measurements were performed on four unreacted Nb_3Sn strands. Three of the strands were tested in the non-straightened configuration (wavy, bent, and

twisted) and one strand was straightened prior to testing. The pre-straightened strand was rolled with a thick steel rod and then straightening by hand. Note that straightening such a bent strand may cold work the material and apply localized stress that could change the mechanical properties. Therefore, these measurements were meant to qualitatively rather than quantitatively assess the validity of performing tensile tests on non-straight samples.

For all tests, E_o was measured at the steepest point in the stress-strain curve and E_u was measured from the entire unloading curve. The mean Young's moduli for the three non-straightened strands were E_o = 28.6 GPa and E_u = 71.3 GPa. The results for the single pre-straightened strand were E_o = 55.8 GPa and E_u = 74.1 GPa.

The stress-strain curves of one of the non-straightened unreacted strands and the pre-straightened unreacted strand are shown in Figure 13. The curve for the pre-straightened strand shows the expected shape of a ductile metal and has a steep initial linear elastic region. In contrast, the steepest portion of the curve for the non-straightened strand occurred between 0.2-0.3% strain. The difference in the initial portions of the stress-strain curves may be due to the straightening of the wavy strand during testing. However, even the pre-straightened strand exhibited a very low value of E_o. Studies have shown that unreacted strands typically have a similar Young's modulus to that of reacted strands (approximately 100-110 GPa), despite differences in ductility between the materials [18]. However, the measured values of E_o deviated from the those cited

in literature [18] by 72.0% for the non-straightened strands and 45.3% for the pre-straightened strands.

The measured values of E_u also deviated significantly from the expected values. This may be due to the fact that the initial twisted configuration of the strand prevented the strand from ever becoming completely straight during testing. The sample grips were fixed, and therefore did not allow the strand to untwist as the axial load was applied. Additionally, the results from all tests violated the condition in IEC Standard 61788-6 (Equation 6) that $\Delta = 0.3$, due to the deviation between E_o and E_u.

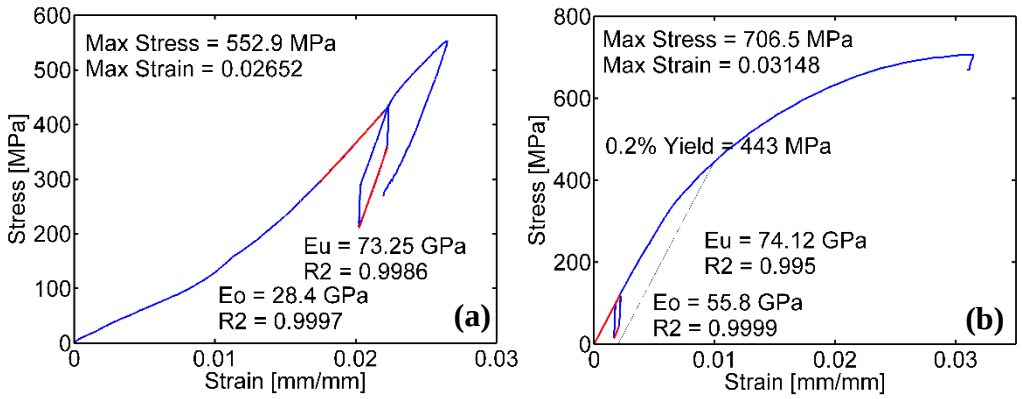

Figure 13: Stress-strain curve of (a) a non-straightened (wavy, bent, and twisted) and (b) a pre-straightened unreacted Nb_3Sn strand.

The differences in the results for the non-straightened and pre-straightened strands suggest that the initial configuration of the strand has a significant effect on the elastic properties. The deviation between the measured properties of the Mevion samples and those found in literature suggests that these properties are not characteristic of the material. Therefore, it was concluded that the unreacted strands provided by Mevion are not appropriate for tensile testing.

3.4 Reacted Nb_3Sn Cables

Ten reacted Nb_3Sn cables were tested, and E_o and E_u for each cable are shown in Table 8. Seven of the tests resulted in premature fracture of the cable at the sample grips (#1, 2, 3, 5, 8, 9 and 10) due to stress concentrations. As a result, the strength at fracture (S_u) was highly variable and therefore has not been reported. The remaining three tests (#4, 6 and 7) ultimately resulted in slippage of the cable within the sample grips. Unloading stress-strain curves were measured for the five samples (#4, 6, 7, 9 and 10) that reached a strain higher than 0.3%. None of the samples reached a high enough strain to calculate the yield strength ($S_{Y0.2\%}$) using the 0.2% offset method, either because of sample slippage or premature fracture.

Table 8: E_o and E_u for individual reacted Nb_3Sn cables.

Sample	#1	#2	#3	#4	#5	#6	#7	#8	#9	#10
E_o [GPa]	59.49	60.61	58.25	61.76	62.69	58.76	56.63	68.32	66.62	59.80
E_u [GPa]	--	--	--	114.22	--	110.05	110.59	--	118.76	116.68

The mean, standard deviation, and coefficient of variation for E_o (Table 9) were calculated from the results of all ten tests. The values for E_u were calculated from the results of the tests in which the cable was unloaded (#4, 6, 7, 9 and 10). The coefficients of variation for E_o and E_u were low (6.04% and 3.31% respectively), showing good consistency between the results for all cables.

Table 9: Mean, standard deviation, and coefficient of variation for E_o and E_u for the reacted Nb_3Sn cables.

	Mean	Standard deviation	Coefficient of variation
E_o [GPa]	61.29	3.70	0.0604
E_u [GPa]	114.06	3.78	0.0331

The mean and standard deviation of the stress was evaluated as a function of strain for all ten cables, as shown in Figure 14a. The maximum standard deviation was 4.57 MPa. A stress-strain curve for one of the cables that was unloaded is shown in Figure 14b. The stress-strain curves for the reacted cables lack the well-defined narrow linear elastic region that is characteristic of the reacted strands.

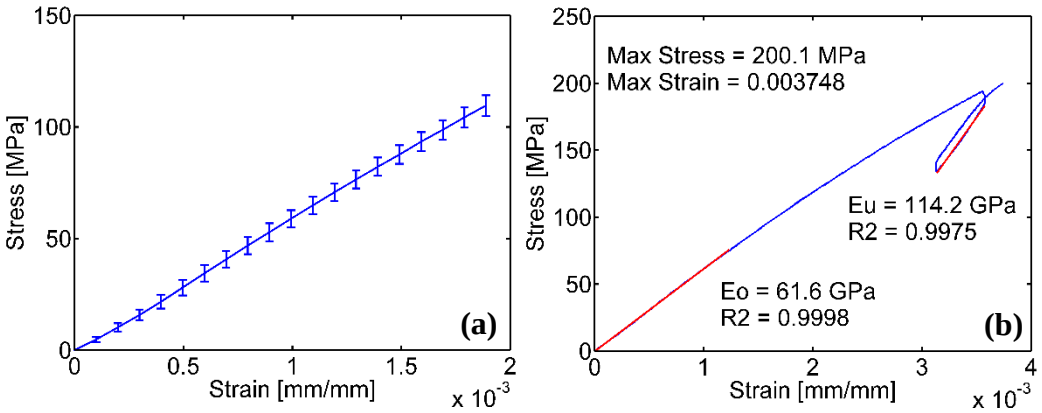

Figure 14: (a) Mean (curve) and standard deviation (error bars) of the stress-strain curves for the reacted Nb_3Sn cables and (b) a stress-strain curve for reacted cable #4.

3.5 Unreacted Nb_3Sn Cables

Measurements were performed on ten unreacted cables, and E_o, E_u and $S_{Y0.2\%}$ for each cable are shown in Table 10. Unloading stress-strain curves were obtained in each test since all cables reached a strain greater than 0.3%. Three of the tests resulted in slippage of the cable within the sample grips (#6, 8 and 10).

The remaining tests were terminated when the applied load reached 90% of the rated capacity of the load cell in order to avoid damaging the equipment. All of the cables except for two (#8 and 10) reached a high enough level of strain to calculate $S_{Y0.2\%}$ using the 0.2% offset method. S_u was not measured since the cables could not be tested until fracture. A load cell with a larger load capacity would need to be installed on the tensile testing apparatus to measure the entire stress-strain curve.

Table 10: E_o, E_u, and $S_{Y0.2\%}$ for the unreacted Nb_3Sn cables.

Sample	#1	#2	#3	#4	#5	#6	#7	#8	#9	#10
E_o [GPa]	66.66	68.50	62.47	65.14	64.60	67.92	64.74	62.29	65.32	65.55
E_u [GPa]	99.46	102.03	98.35	96.51	105.26	104.39	104.56	103.66	99.74	104.33
$S_{Y0.2\%}$ [MPa]	423.56	401.45	439.50	415.84	444.98	403.42	418.86	--	430.10	--

The mean, standard deviation, and coefficient of variation of E_o, E_u, and $S_{Y0.2\%}$ are shown in Table 11. The values were calculated based on all of the data included in Table 10. Like the results from the reacted cables, the coefficients of variation for E_o, E_u and $S_{Y0.2\%}$ were quite low (3.10%, 3.03%, and 3.71% respectively), showing good consistency between the results for different cables.

Table 11: Mean, standard deviation, and coefficient of variation of E_o, E_u, and $S_{Y0.2\%}$ for the unreacted Nb_3Sn cables.

	Mean	Standard deviation	Coefficient of variation
E_o [GPa]	65.32	2.03	0.0310
E_u [GPa]	101.83	3.09	0.0303
$S_{Y0.2\%}$ [MPa]	422.21	15.66	0.0371

The mean and standard deviation of the stress as a function of strain for all ten tests show that there is very little variation in the stress-strain curves (Figure

15a). The maximum standard deviation was 6.18 MPa. A stress-strain curve for one of the unreacted cables (sample #2) is shown in Figure 15b.

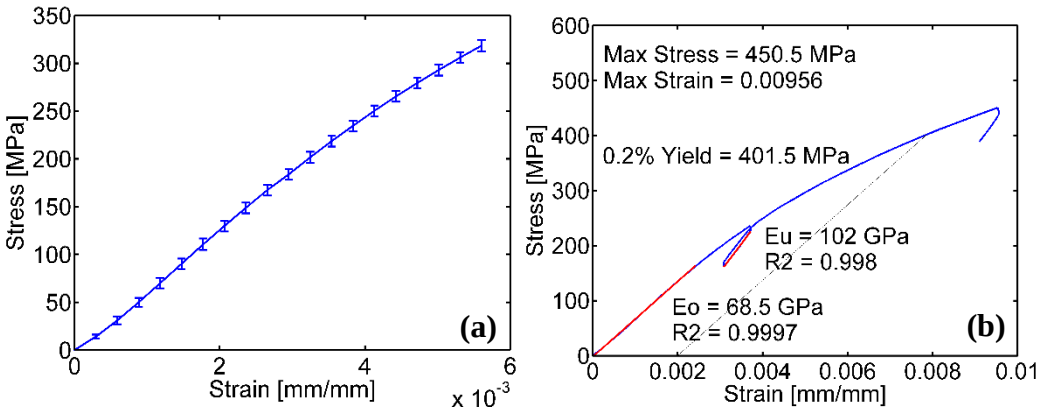

Figure 15: Mean (curve) and standard deviation (error bars) of the stress as a function of strain for the unreacted cables and (b) the stress-stain curve for unreacted cable #2.

3.6 Discussion and Summary of Experimental Results

The results from the tests on the reacted Nb_3Sn strands, reacted Nb_3Sn cables, and unreacted Nb_3Sn cables are summarized in Table 12. The results for the unreacted Nb_3Sn strands have been omitted for the reasons discussed in Section 3.3.

Prior studies have shown that the heat treatment of Nb_3Sn tends to result in a marginal increase in the Young's modulus of the material [18]. This could not be confirmed for the Mevion strands since valid results were not obtained for the unreacted strands. For the cables, heat treatment did increase the mean value of E_u from 99.09 GPa to 114.06 GPa, but decreased the mean value of E_o from 65.70 GPa to 61.29 GPa. However, considering that the definition of E_o and E_u is different for a cable than a single strand, it is difficult to make such comparisons.

Other factors besides the change in the Young's modulus of the material due to heat treatment may have influenced the values of E_o and E_u for the cable. For example, the increase in the diameter of the individual strands in the cable or changes of the coefficient of friction between strands as a result of heat treatment may have affected the cable stiffness.

Table 12: Summary of the mechanical properties of the reacted Nb3Sn strands, reacted Nb3Sn cables, and unreacted Nb3Sn cables.

Material	Property	Mean	Standard deviation	Coefficient of variation
Reacted strand	E_o [GPa]	93.5	12.7	0.136
	E_u [GPa]	123.4	10.4	0.084
	S_u [MPa]	253.7	4.1	0.016
Reacted cable	E_o [GPa]	61.29	3.70	0.060
	E_u [GPa]	114.06	3.78	0.033
Unreacted cable	E_o [GPa]	65.70	2.55	0.039
	E_u [GPa]	99.09	2.31	0.023
	$S_{Y0.2\%}$ [MPa]	420.09	15.86	0.038

The largest coefficient of variation for the measured mechanical properties was of E_o for the reacted strands. All other coefficients of variation were less than 10%. Coefficients of variation were consistently larger for E_o than for E_u for all sample types. The international round robin test also found larger coefficients of variation for E_o than for E_u for reacted Nb_3Sn strands, which they attributed to the small elastic limit of the stress-strain curve [16]. Other studies have attributed the scatter in E_o for strands to prebending and handling of the sample [16], [17]. In general, E_u is considered to be a more accurate measure of the Young's modulus.

The scatter in E_o is the primary reason for the variation between E_o and E_u. To quantify this variation, Δ_a was calculated for each sample that was unloaded. For the reacted Nb_3Sn strands, only one sample violated the condition established by IEC Standard 61788-6 that $\Delta = 0.3$. The condition was violated by all of the

reacted and unreacted cables. However, it should be acknowledged that IEC Standard 61788-6 directly applies only to reacted Nb_3Sn strands. Interestingly, the calculated values of Δ_a were quite consistent for the reacted and unreacted cables, as shown by low coefficients of variation in Table 13. This suggests that it may not be valid to assume that E_o and E_u are equal for cables under ideal conditions.

Table 13: Δ_a for the reacted and unreacted cable samples. Calculations are based on the samples for which both E_o and E_u were measured.

	Mean	Standard deviation	Coefficient of variation
Reacted cable	0.532	0.021	0.039
Unreacted cable	0.663	0.019	0.028

For comparison, the stress-strain curves for a single reacted strand, reacted cable, and unreacted cable are shown in Figure 16. As shown, the stress-strain behavior of the reacted stand and cable were very similar, except at very low strains. The reacted strand stress-strain curve is from one of the samples that fractured in the middle of the strand, so the maximum point can be interpreted as the fracture strength. However, the maximum points on the stress-strain curves for the reacted and unreacted cables in Figure 16 should not be interpreted as fracture strengths.

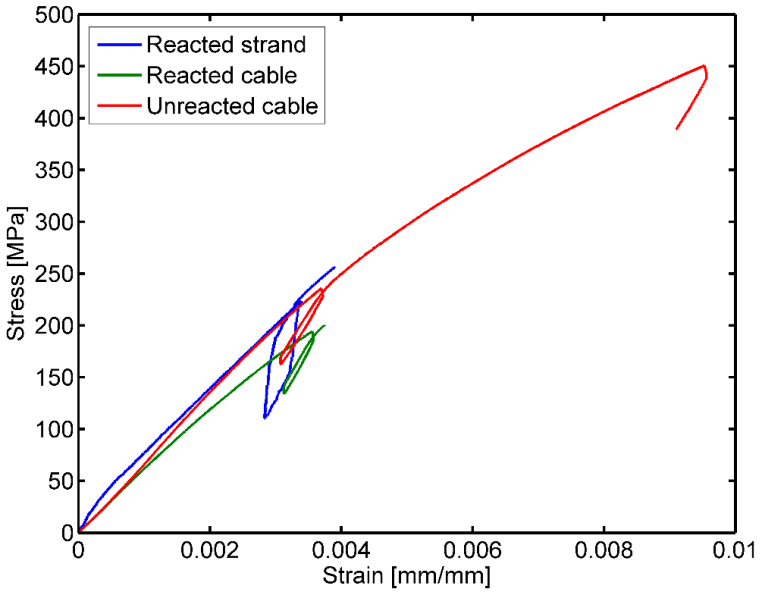

Figure 16: Comparison of the stress strain curves of a reacted strand, reacted cable, and unreacted cable.

All samples in this study fractured at the inside edge of the sample grips or between the gripping plates of the sample grips, except for two of the reacted Nb_3Sn strands. As previously discussed, breakage in these locations is indicative of premature fracture from stress concentrations. The brittle nature of the reacted samples made it challenging to hold the strand or cable with a sufficient force to prevent slipping, but also avoid stress concentrations that exceed the fracture strength of the material. Stress concentrations may have arisen due to the clamping force applied to the gripping plates, small deformations from handling and mounting the sample, or slight misalignment of the sample grips that could not be observed from visual inspection. Other similar studies have also reported a high occurrence of fracture at the sample grips [19], [24]. The short sample lengths (65 mm) of the reacted Nb_3Sn strands may have worsened any misalignment of the sample grips. Future measurements should use longer sample

lengths that adhere to the recommendations of IEC Standard 61788-6. In order obtain values of S_u for the reacted and unreacted cables, the sample grips may need to be redesigned to prevent any sample slippage and reduce stress concentrations.

4. Analytical Results and Discussion

The Nb_3Sn cables from Mevion are structurally similar to the metallic cables used in a variety of non-superconducting applications, such as concrete construction and rubber tire reinforcement. The mechanical behavior of these types of cables has been heavily studied over the last century, and numerous numerical models have been developed. Within the field of mechanics, these types of cables are referred to as wire ropes. Numerical models in this area of study are generally specific to either single helix cables, double-helix cables, or cables with more complex configurations. Single helix cables are made up of several strands twisted around a center wire, such as the cables considered in this study. Double-helix cables consist of multiple single-helix sub-cables twisted around a single helix core sub-cable. Configurations become more complicated if cables have multiple layers of twisted strands. After reviewing the literature on the mechanics of wire ropes, two analytical models that are applicable to the Nb_3Sn cables from Mevion were selected. These models were used to calculate the effective Young's modulus of the cable, which was compared to the empirical results in Section 3. Literature on wire ropes generally follows different naming conventions than the field of superconductivity for the terms cable, wire, rope, and strand. To avoid confusion, the naming conventions used so far will continue to be used.

4.1 Model 1: Costello and Phillips

Costello and Phillips developed much of the foundational work on wire ropes [25], [26]. Their work expands on the theory published by A. E. H Love in 1944 on the bending and twisting of thin rods [27]. In this section, the theory developed by Costello for a straight cable [25] is applied to the reacted Mevion cable and used to estimate the effective Young's modulus.

Figure 17a shows the cross-section of the reacted Mevion cable based on the assumptions of Costello's model. R_1 is the radius of the center wire, R_2 is radius of the side strands, and R_H is the radius of the helix formed by the side strands. The drawing is proportional to the average dimensions of the heat treated cables (R_1 = 0.1465 mm and R_2 = 0.3929 mm) which differed from the nominal dimensions provided by Mevion (Figure 2). In the unloaded condition, the side strands are in contact with each other but are not in contact with the center wire. The cross-section of the side strands of the cable are elliptical in the plane normal to the axis of the center wire, due to the helical path of the side strands. Costello assumes that the cross section of each strand remains circular along its axis during loading, and there are no deformations due to contact forces. The model accounts for the reduction in the diameter of individual strands from axial displacement due to the Poisson effect.

The helix angle α of the side strands can be calculated from the cable pitch P and the helix radius R_H:

$$tan(\alpha) = \frac{P}{2\pi R_H} \tag{10}$$

For a cable in which the side strands are in contact with each other, R_H can be calculated from [25]:

$$R_H = R_2\left[1 + \frac{tan^2(\frac{\pi}{2}-\frac{\pi}{m})}{sin^2\,\alpha}\right]^{\frac{1}{2}} \tag{11}$$

where m is the number of side strands. Equations 10 and 11 are a system of two equations with two unknowns (α and R_H). For P = 20 mm and m = 4, it is found that α = 80.02° and R_H = 0.5599 mm.

Given a cable strain ε and assuming that the change in the helix angle from loading is small and the ends of the ends of the strand cannot rotate, the following system of equations can be solved to find the strain of the center wire (ξ_1), strain of the side strands (ξ_2) and the helix angle after loading ($\bar{\alpha}$) [25]:

$$\varepsilon = \xi_2 + \frac{\bar{\alpha}-\alpha}{tan\,\alpha} \tag{12}$$

$$0 = \frac{\xi_2}{tan\,\alpha} - (\bar{\alpha} - \alpha) + \upsilon\frac{(R_1\xi_1+R_2\xi_2)}{R_H\,tan\,\alpha} \tag{13}$$

$$\xi_1 = \varepsilon \tag{14}$$

The free-body diagram in Figure 17b shows the forces acting on a small element of a side strand. An orthogonal coordinate system is defined such that the x and y directions are in the plane of the strand cross-section and the z direction is normal to the cross-section. N and N' are the shearing forces on the strand cross-section in the x and y directions, T is the tensile force in the z direction, G and G' are the bending moments on the cross-section in the x and y directions, H is the twisting moment in the z direction, X, Y, and Z are external forces in the x, y, and z directions per unit length, and K, K', and θ are the external moments in the x, y, and z directions per unit length.

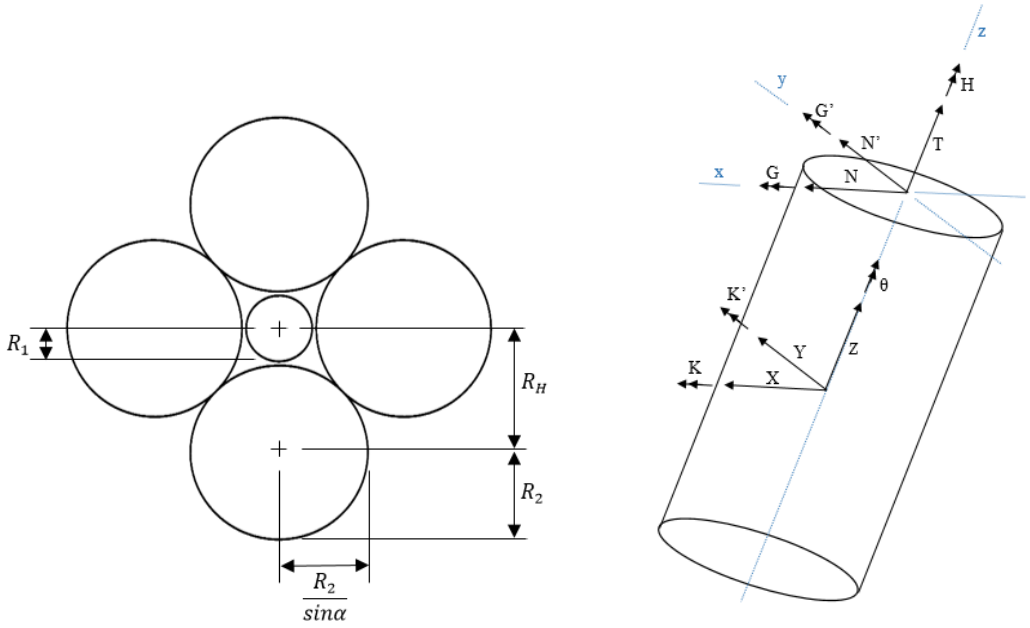

(a) **(b)**

Figure 17: (a) Geometric parameters of a reacted Nb_3Sn cable prior to loading and (b) a force-body diagram showing the forces acting on the cross-section of a side strand.

The static response of a straight cable to a tensile load in the axial direction with no bending is defined by Costello with the following equilibrium (15-17) equations for the forces in the x, y, and z directions [25]. $\bar{\tau}_2$ is the twist per unit length of the side strand, and $\bar{\kappa'}_2$ is the component of curvature of the side strand in the y direction after loading. It is assumed that there are no frictional forces between strands.

$$\Sigma F_x: \quad -N'_2\bar{\tau}_2 + T_2\bar{\kappa'}_2 + X_2 = 0 \tag{15}$$
$$\Sigma F_y: \quad Y_2 = 0 \tag{16}$$
$$\Sigma F_z: \quad Z_2 = 0 \tag{17}$$

Similarly, the equilibrium equations for the moments in the x, y, and z directions are:

$$\Sigma M_x: \quad -G'_2\bar{\tau}_2 + H_2\bar{\kappa}'_2 + N'_2 = 0 \tag{18}$$
$$\Sigma M_y: \quad N_2 = 0 \tag{19}$$
$$\Sigma M_z: \quad \Theta_2 = 0 \tag{20}$$

The total axial force on the cable (F) is the sum of the axial force applied to the center wire (F_1) plus the axial force applied to the side strands (F_2):

$$F = F_1 + F_2 \tag{21}$$

F_1 is defined as:

$$F_1 = \pi {R_1}^2 E_1 \xi_1 \tag{22}$$

where E_1 is the Young's modulus of the center wire. F_2 is defined as:

$$F_2 = m_2(T_2 \sin\alpha + N'_2 \cos\alpha) \tag{23}$$

where:

$$T_2 = \pi \xi_2 E_2 R_2 \tag{24}$$

$$N'_2 = H_2 \frac{\cos^2\alpha}{R_H} - G'_2 \frac{\sin\alpha\cos\alpha}{R_H} \tag{25}$$

$$H_2 = \frac{\pi E_2 {R_2}^3}{4(1+\nu)} \left[\frac{(1-2\sin^2\alpha)}{\frac{R_H}{R_2}} (\bar{\alpha} - \alpha) + \upsilon \frac{(R_1\xi_1 + R_2\xi_2)}{R_H} \frac{\sin\alpha\cos\alpha}{\frac{R_H}{R_2}} \right] \tag{26}$$

$$G'_2 = \frac{\pi}{4} R_2 {E_2}^3 \left[\frac{-2\sin\alpha\cos\alpha}{R_H/R_2} (\bar{\alpha} - \alpha) + \nu \frac{(R_1\xi_1 + R_2\xi_2)}{R_H} \frac{\cos^2\alpha}{\frac{R_H}{R_2}} \right] \tag{27}$$

E_2 is the Young's modulus of the side strands. The derivation of these equations is based on the equilibrium equations (15-20) and is fully described by Costello [25]. The cable stress in the axial direction can be calculated by dividing F by the metallic area of the cable A_m, which is the sum of the initial cross sectional areas of the individual strands. Since the helix angle is large, the elliptical cross sectional area of the side strand in the plane normal to the cable axis can be closely approximated by the circular area in the plane normal to the strand axis.

$$A_m = 4\pi(R_2)^2 + \pi(R_1)^2 \quad (28)$$

In this analysis, it was assumed that the behavior of the strands is entirely elastic. Therefore the modeled stress-strain curve is linear for all values of strain, and the slope is equal to the effective Young's modulus of the cable (E_c). For the reacted Mevion cable, it was assumed that E_1 = 110 GPa, a typical value for copper [23], and E_2 = 93.5 GPa, the average empirical value of E_o for the reacted Nb_3Sn strands. The Poisson ratio was set equal to ν = 0.34 which is a normal value for copper [23]. Based on this analysis, E_c was calculated to be 89.2 GPa. A 10% increase in E_1 resulted in a 0.4% increase in E_c, suggesting that the contribution of the center wire to the overall cable stiffness is small. However, a 10% increase in E_2 resulted in a 9.6% increase in E_c.

4.2 Model 2: Wu and Cao

Wu and Cao [28] developed a theoretical model for a double-helix cable with multiple layers that is based on the theory developed by Costello [25] but uses slightly different assumptions. This model was simplified here in order to be applied to a single-layer, single-helix cable, and was used to evaluate the effective Young's modulus of the reacted Nb_3Sn cable. Like Costello [25], Wu and Cao assume that there is no friction between the individual strands of the cable and they account for the change in the strand diameter due to the Poisson effect. A primary difference between the models is that Wu and Cao assume that cross-sections of the side strands are circular rather than elliptical in the plane normal to

the cable axis, as shown in Figure 18. From Equation 10, the helix angle was calculated to be α = 80.10°, which is negligibly different from the helix angle calculated in the previous section.

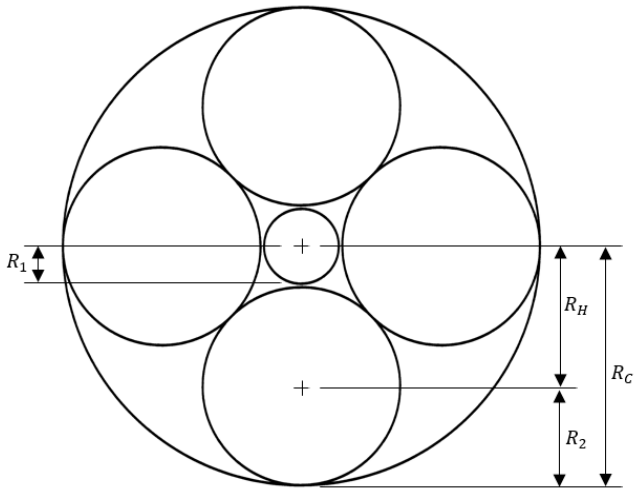

Figure 18: Mevion cable cross-section assuming circular cross-sections of the side strands.

In this model, the definition of R_1 and R_2 remain the same and R_c is the outer radius of the cable. From the geometry in Figure 18, the helix radius is equal to:

$$R_H = \frac{2R_2}{\sqrt{2}} \tag{29}$$

In the analysis of the previous model by Costello, it was assumed that the ends of the cable are not able to rotate. In this analysis, the ends of the cable are allowed to rotate. The constitutive equations used to relate the curvature of the side strands to the loads on the side strands also differ between the two models. Ramsey [29] showed that Costello misinterpreted the theory developed by Love [27], such that relative rotation of the strands with respect to each other is not

allowed in Costello's model. Ramsey developed improved equations, which are utilized by Wu and Cao in their analysis.

Wu and Cao derive the following approximation for E_c for a multilayered cable:

$$E_c \approx \left(\frac{R_1}{R_c}\right)^2 E_1 + \sum_{i=2}^{n} m_i \left(\frac{R_i}{R_c}\right)^2 E_i \sin \alpha_i \quad (30)$$

where n is the layer of the cable, R_i is the radius of the side strands in the i^{th} layer, E_i is the Young's modulus of the side strands in the i^{th} layer, m_i is the number of side strands in the i^{th} layer, and α_i is the helix angle of the side strands in the i^{th} layer. Since the Mevion cable is a single-helix and has a single layer of side strands, n = 2.

In the derivation of Equation 30, it is assumed that the area of the cross-section of the cable is equal to the area of the outer circle tangent to the side strands of the cable:

$$A = \pi(R_c)^2 \quad (31)$$

However, the metallic area of the cable A_m, which was defined in Equation 28, has been used to calculate the stress in the cable up until this point in this study. Using A_m in the calculation of E_c is more accurate since A_m is the area to which the axial force is applied during tensile testing. To account for this definition of the area in the model and to be constant with the empirical results, an effective radius of the cable R_e was calculated such that:

$$A_m = \pi(R_e)^2 \quad (32)$$

By substituting R_e for R_c and setting n=2 for a single layer of side strands in the cable, Equation 30 can be simplified to:

$$E_c \approx \left(\frac{R_1}{R_e}\right)^2 E_1 + m\left(\frac{R_2}{R_e}\right)^2 E_2 \sin\alpha \tag{33}$$

For m = 4, R_c = 0.953 mm, and R_e = 0.780 mm, E_c was calculated to be 92.7 GPa. Increasing E_1 by 10% resulted in an increase in E_c of 0.4%, again suggesting that the contribution of the center wire to the elastic behavior of the cable is relatively small.

4.3 Discussion of Analytical Results

The effective Young's moduli of the reacted cable that were calculated from the two analytical models (89.2 GPa and 92.7 GPa respectively) show only a slight reduction of the Young's modulus of the cable relative to a single Nb_3Sn strand. The analytical values of E_c are between the empirical values of E_o (65.70 GPa for the unreacted cable, 61.29 GPa for the reacted cable) and E_u (101.83 GPa for the unreacted cable, 114.06 GPa for the reacted cable), but agree more closely with the values for E_u. This supports the finding in other studies that empirical results for E_u are generally more representative of the Young's modulus of the material than E_o [17]. Factors such as the initial bent configuration of the cable and the mounting of the cable may have contributed to the low empirical value of E_o.

The two models produced very similar results despite using different assumptions for the end rotation of the strand, the kinematic relations between

strands, and the cross-sectional geometry. The effect of contact deformation between strands was not considered in this analysis, but could be considered for greater accuracy. It may also be important to consider the effects of friction, since the side strands of the cable are always in contact with each other. The analysis was only applied here to a reacted cable due to the lack of verifiable data for the unreacted strands. However, the same analytical models could be applied to the unreacted cable if the Young's modulus of the unreacted strands was obtained from further testing.

It is important to note that the analytical calculation of the effective Young's modulus of the cable is highly dependent on the definition of the cross-sectional area. Here, the area was defined as the metallic area, or the sum of the initial areas of the cross-sections of the individual strands. Using the area of the outer circle of the cable would have led to values of the effective Young's modulus of the cable that were 29.6% lower than the current results. From a review of the literature, there does not seem to be a consensus regarding the appropriate definition of the area, with some studies using the metallic area and others using the net cable area. Any comparison between analytical or empirical results of different studies should account for differences in the area calculation.

5. Conclusions

Tensile tests were performed on reacted and unreacted Nb_3Sn strands and cables, and the stress-strain curves were used to calculate E_o, E_u, $S_{Y0.2\%}$, and S_u, whenever possible. All of the results exhibited a coefficient of variation below 10%, except for E_o for the reacted strands. Measured values of E_o tended to exhibit greater scatter than the values for E_u, which is consistent with the findings of other studies. The larger coefficient of variation for E_o may be attributed to handling of the sample and testing from a slightly bent configuration.

For the reacted strands, the average empirical results for E_o, E_u, and S_u were within 10% of literature results for a similar material. The fracture strength was obtained from the measurements of samples that fractured in the middle of the strand, rather than at the sample grips. Stress-strain curves exhibited a characteristic narrow linear elastic region that extended to 0.2-0.3% strain.

The provided unreacted strands were initially wavy, bent and twisted, having been unwound from a cable. This configuration was not suitable for tensile testing. Differences between in the stress-strain behavior of the pre-straightened and non-straightened unreacted strands suggest that the initial configuration of the strand does significantly affect the stress-strain behavior. Deviations between the measured results and literature values suggests that the results obtained from these strands are not characteristic of the intrinsic material properties.

For the cables, there was considerable deviation between E_o and E_u, resulting in average values of Δ_a of 0.532 and 0.663 for the reacted and unreacted samples, respectively. While stress-stain curves for the reacted strands exhibited a

clear transition between the elastic and plastic regions, the two regions were much less defined for the reacted cables.

The effective Young's modulus E_c of the reacted cable was evaluated analytically with two different theoretical models from literature on the mechanics of wire ropes. The calculated value of E_c for the two models (89.2 GPa and 92.7 GPa) differed by 3.9%, showing good agreement. The results indicate only a slight reduction in the Young's modulus of the cable relative to a single strand. The sensitivity of E_c to the Young's modulus of the center wire was small. The analytical values of E_c were closer to the empirical values of E_u than E_o. This supports the concept that E_u is generally considered to be a more accurate representation of the Young's modulus of the material.

5.1 Future Work and Recommended Improvements to the Tensile Testing Apparatus

The LVDT was used to measure the strain applied to the cable samples, since it was not possible to mount the extensometers on the cable. A bias factor was used to account for the overall compliance of the tensile testing apparatus. However, the determination of the bias factor introduces an additional source of uncertainty into the calculations. A direct measurement of the cable strain that does not require knowledge of the compliance of the apparatus would improve the accuracy of the strain measurements. Clip-on extensometers with a gauge length equal to the twist pitch of the cable could be used for this purpose. Non-contact

displacement sensing, such as video or optical extensometers, could also be used to directly measure the cables strain with high precision.

Slack in the tensile testing apparatus (34.1 - 42.4 N) was observed at the point of unloading from the load cell measurements. The drop in the load at the point of unloading limited the portion of the unloading stress-strain curve that could be measured. IEC Standard 61788-6 recommends using the region between 99% and 90% of the applied load at the point of unloading to calculate E_u, requiring a sharp transition between the loading and unloading curves. It was found that the slack in the apparatus was reduced by 88.5% by disabling the LVDT. However as previously described, the LVDT was required to measure the strain applied to the cables. Future work should investigate whether the slack is attributed to the mounting of the LVDT on the tensile testing apparatus or the sliding mechanism within the LVDT, and make the appropriate modifications or replacements.

The unreacted cables were not tested until fracture to avoid exceeding the rated maximum capacity of the load cell of 1112 N (250 lbf). For future measurements, a load cell with a larger capacity should be installed so that the entire stress-strain curve may be obtained. A 2224 N (500 lbf) load cell would be appropriate to both reach the fracture strength of the cable and provide good measurement resolution.

The results were based on a sample size of six for the reacted strands, ten for the reacted cables, and ten for the unreacted cables. Additional tests on the same materials would improve the statistical significance of the results, and help

to characterize the distribution of mechanical properties for each sample type more accurately

Since the mechanical properties of Nb_3Sn are dependent on temperature, additional tests could be performed at cryogenic temperatures to provide data that is more applicable to the operating conditions of LTS superconducting magnets. In general, the values of the mechanical properties of Nb_3Sn are greater at cryogenic temperatures than at room temperature. The tensile testing apparatus used in this study was originally designed for use in a liquid nitrogen cryostat, so tests could be conducted at 77 K using the same instrumentation. To conduct tests at 4.2 K, liquid helium could be used as a cryogen, although the difference between the mechanical properties at 77 K and 4.2 K is generally minimal.

6. References

[1] *Mevion Medical Systems*. [Online]. Available: http://www.mevion.com/.

[2] C. P. Poole, H. A. Farach, R. J. Creswick, and R. Prozorov, *Superconductivity*, 3rd ed. Elsevier Science.

[3] R. G. Sharma, *Superconductivity: Basics and Applications to Magnets*, vol. 214. Springer, 2015.

[4] A. Devred *et al.*, "Challenges and status of ITER conductor production," *Supercond. Sci. Technol.*, vol. 27, pp. 1–39, 2014.

[5] G. Apollinari, S. Prestemon, and A. V. Zlobin, "Progress with High-Field Superconducting Magnets for High-Energy Colliders," *Annu. Rev. Nucl. Part. Sci.*, vol. 65, pp. 355–377, 2015.

[6] D. L. Friesel and T. A. Antaya, "Medical cyclotrons," *Rev. Accel. Sci. Technol.*, vol. 2, no. 01, pp. 133–156, 2009.

[7] R. Jayakumar, *Particle Accelerators, Colliders, and the Story of High Energy Physics*. Springer, 2012.

[8] H. G. Blosser, B. F. Milton, J. Riedel, and M. Riedel, "Superconducting Synchrocyclotron," 4,641,057, 03-Feb-1987.

[9] H. Owen, D. Holder, J. Alonso, and R. Mackay, "Technologies for delivery of proton and ion beams for radiotherapy," *Int. J. Mod. Phys. A*, vol. 29, no. 14, p. 1441002, 2014.

[10] J. Flanz and T. Bortfeld, "Evolution of Technology to Optimize the Delivery of Proton Therapy: The Third Generation," *Semin. Radiat. Oncol.*, vol. 23, no. 2, pp. 142–148, 2013.

[11] B. T. Matthias, T. H. Geballe, S. Geller, and E. Corenzwit, "Superconductivity of Nb3Sn," *Phys. Rev.*, vol. 95, no. 6, p. 1435, 1954.

[12] J. W. Ekin, "Strain scaling law for flux pinning in practical superconductors. Part 1: Basic relationship and application to Nb3Sn conductors," *Cryogenics*, vol. 20, no. 11, pp. 611–624, 1980.

[13] K. P. Weiss, R. Heller, W. H. Fietz, J. L. Duchateau, N. Dolgetta, and A. Vostner, "Systematic Approach to Examine the Strain Effect on the Critical Current of Nb3Sn Cable-in-Conduit-Conductors," *IEEE Trans. Appl. Supercond.*, vol. 17, no. 2, pp. 1469–1472, 2007.

[14] I. Husek, P. Kovac, and H. Jones, "Tensile stress applied to NbTi, Nb3Sn, Bi-2223 and MgB2 composite superconductors at room temperature," *Supercond. Sci. Technol.*, vol. 17, pp. 1411–1414, 2004.

[15] "IEC 61788-6 Mechanical properties measurement - Room temperature tensile test of reacted Nb3Sn composite superconductors." .

[16] K. Osamura *et al.*, "International round robin test for mechanical properties of Nb3Sn superconductive wires at room temperature," *Supercond. Sci. Technol.*, vol. 21, no. 4, p. 045006, 2008.

[17] K. Katagiri, K. Kasaba, M. Hojo, K. Osamura, M. Sugano, and A. Kimura, "Tensile testing methods of Cu/Nb3Sn superconducting wires at room temperature," *Phys. C*, pp. 1302–1305, 2001.

[18] D. A. Harvey, N. A. Fellows, J. F. Durodola, and A. Twin, "The influence of the reaction heat-treatment process on the mechanical properties of multi-

filamentary composite Nb3Sn superconducting wires at 77 and 300 K," *Supercond. Sci. Technol.*, vol. 19, pp. 79–84, 2006.
[19] A. Nyilas, "Strain sensing systems tailored for tensile measurement of fragile wires," *Supercond. Sci. Technol.*, vol. 18, pp. S409–S415, 2005.
[20] "IEC 61788 Mechanical properties measurement - Tensile test of practical REBCO and BSCCO composite superconductors at cryogenic temperatures." 2016.
[21] D. Bader, "Design, Fabrication, and Testing of an Apparatus for Mechanical Properties Characterization of Nb3Sn Superconducting Wires," Tufts University, Medford, Massachusetts, 2012.
[22] "E8/E8M - 16a Standard Test Methods for Tension Testing of Metallic Materials." ASTM, 2016.
[23] W. D. Callister, Jr. and D. G. Rethwisch, *Materials Science and Engineering: An Introduction*, 9th ed. John Wiley and Sons, 2015.
[24] N. C. van den Eijnden, A. Nijhuis, Y. Ilyin, W. A. J. Wessel, and H. H. J. ten Kate, "Axial tensile stress-strain characterization of ITER model coil type Nb3Sn strands in TARSIS," *Supercond. Sci. Technol.*, vol. 18, pp. 1523–1532, 2005.
[25] G. A. Costello, *Theory of Wire Rope*, 2nd ed. Springer, 1997.
[26] G. A. Costello, M. ASCE, and J. W. Phillips, "Effective Modulus of Twisted Wire Cables," *J. Eng. Mech. Div.*, vol. 102.1, pp. 171–181, 1976.
[27] A. E. H. Love, *A Treastise on the Mathematical Theory of Elasticity*, 4th ed. New York: Dover Publications, 1944.
[28] W. Wu and X. Cao, "Mechanics model and its equation of wire rope based on elastic thin rod theory," *Int. J. Solids Struct.*, vol. 102–103, pp. 21–29, 2016.
[29] H. Ramsey, "A Theory of Thin Rods with Application to Helical Constituent Wires in Cables," *Int. J. Mech. Sci.*, vol. 30, no. 8, pp. 559–570, 1988.

7. Appendix A: Sample Grip Drawings

This section includes the SolidWorks drawings of the sample grips used for the cable measurements. The drawings of the sample grips used for the strand measurements can be found in [21]. The only modifications made to the strand sample grips for the measurements in this study was a reduction in the v-groove depth from 0.015” to 0.014”.

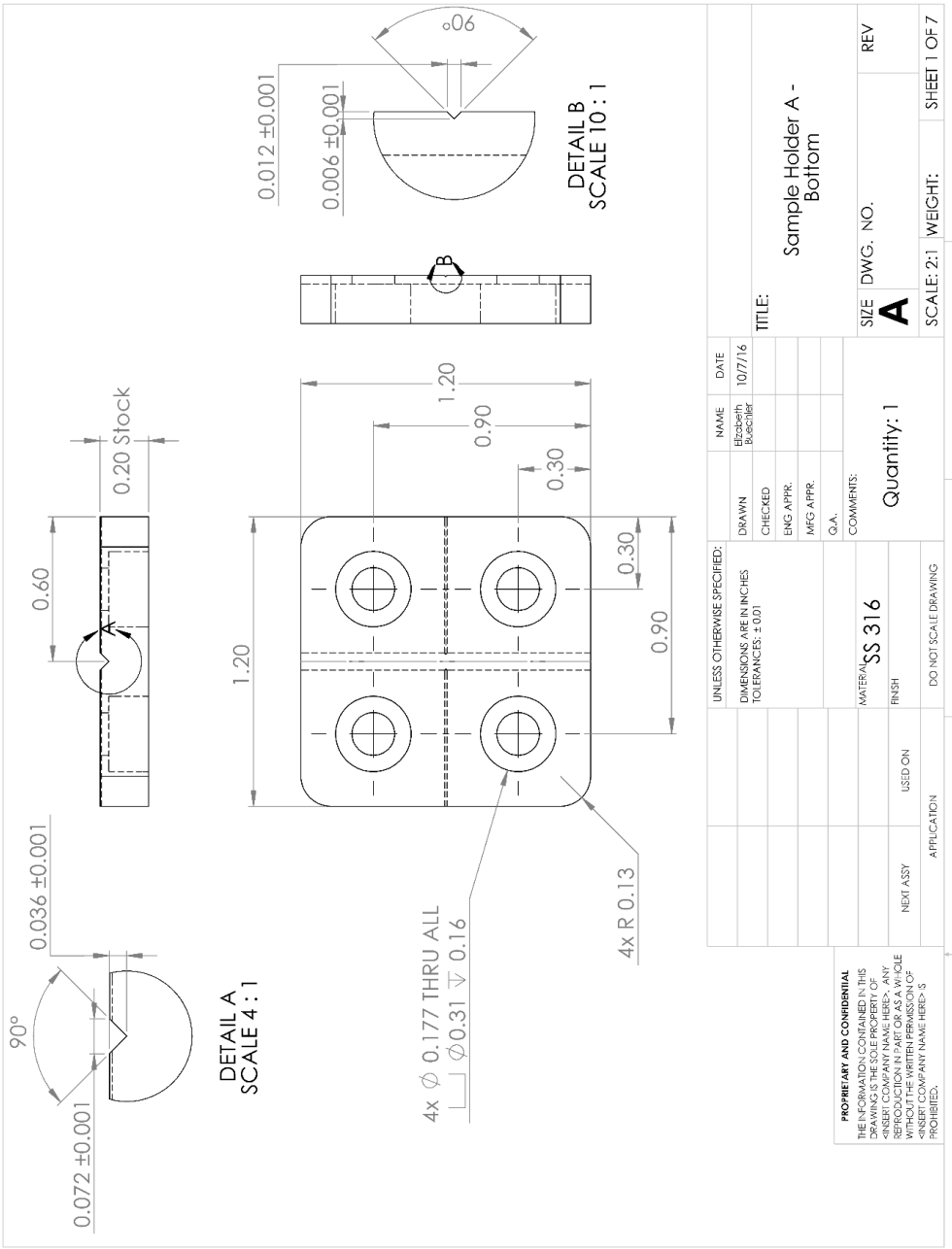

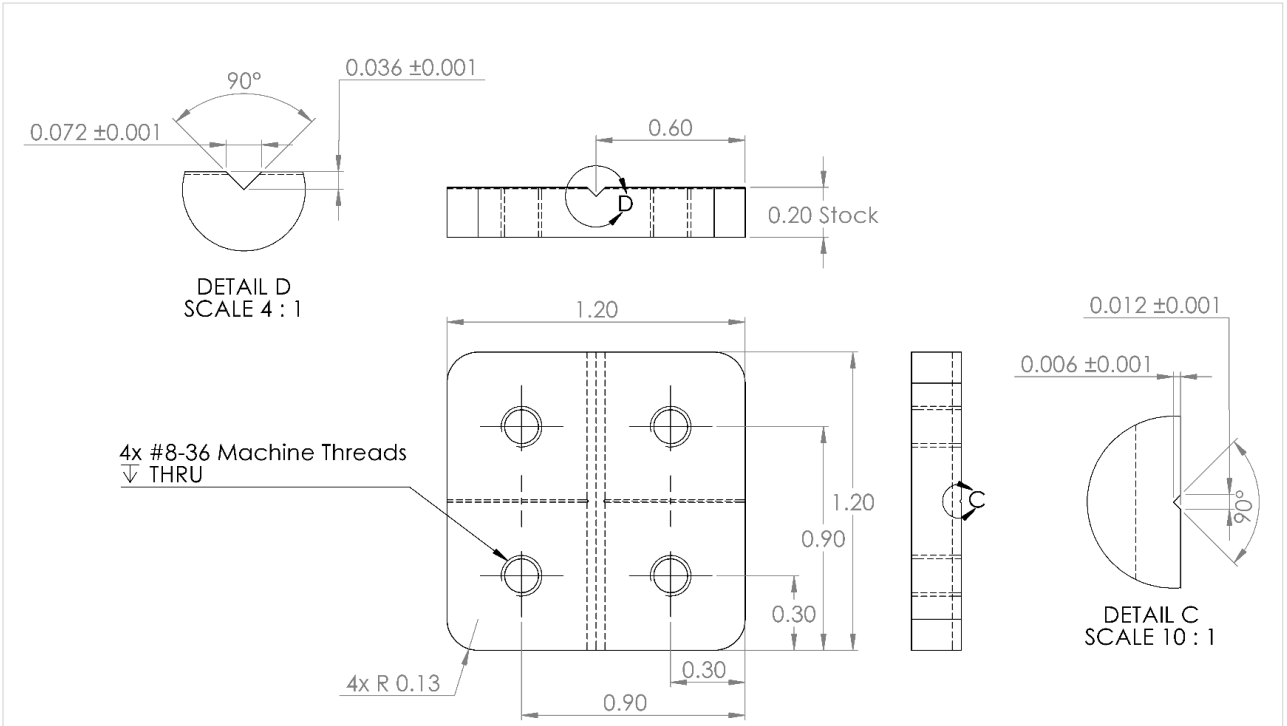

		UNLESS OTHERWISE SPECIFIED:		NAME	DATE
		DIMENSIONS ARE IN INCHES TOLERANCES: ±0.01	DRAWN	Elizabeth Buechler	10/7/16
			CHECKED		
			ENG APPR.		
			MFG APPR.		
			Q.A.		
		MATERIAL SS 316	COMMENTS: Quantity: 1		
NEXT ASSY	USED ON	FINISH			
APPLICATION		DO NOT SCALE DRAWING			

TITLE: Sample Holder B

SIZE A | DWG. NO. | REV

SCALE: 2:1 | WEIGHT: | SHEET 2 OF 7

5 4 3 2 1

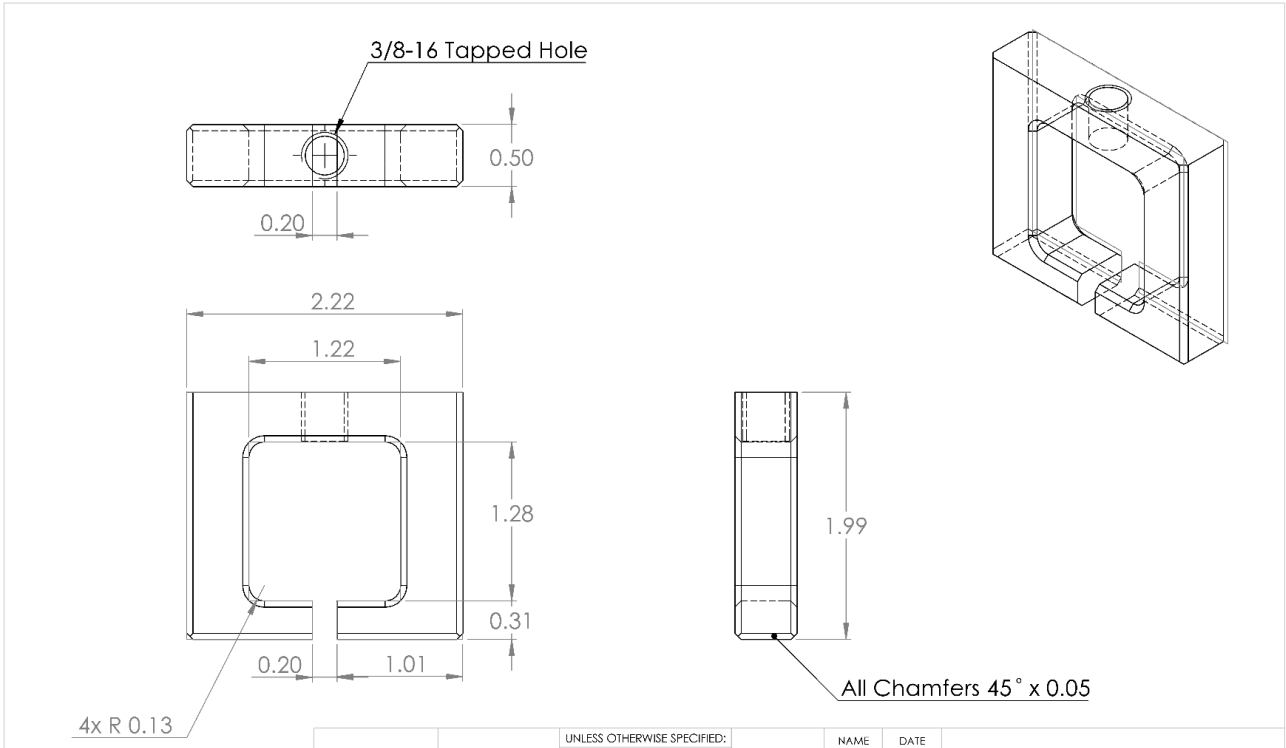

		UNLESS OTHERWISE SPECIFIED:		NAME	DATE
		DIMENSIONS ARE IN INCHES TOLERANCES: ±0.01	DRAWN	Elizabeth Buechler	10/7/16
			CHECKED		
			ENG APPR.		
			MFG APPR.		
			Q.A.		
		MATERIAL SS 316	COMMENTS: Quantity: 1		
NEXT ASSY	USED ON	FINISH			
APPLICATION		DO NOT SCALE DRAWING			

TITLE: Sample Holder C

SIZE	DWG. NO.	REV
A		

SCALE: 1:1 | WEIGHT: | SHEET 3 OF 7

5 4 3 2 1

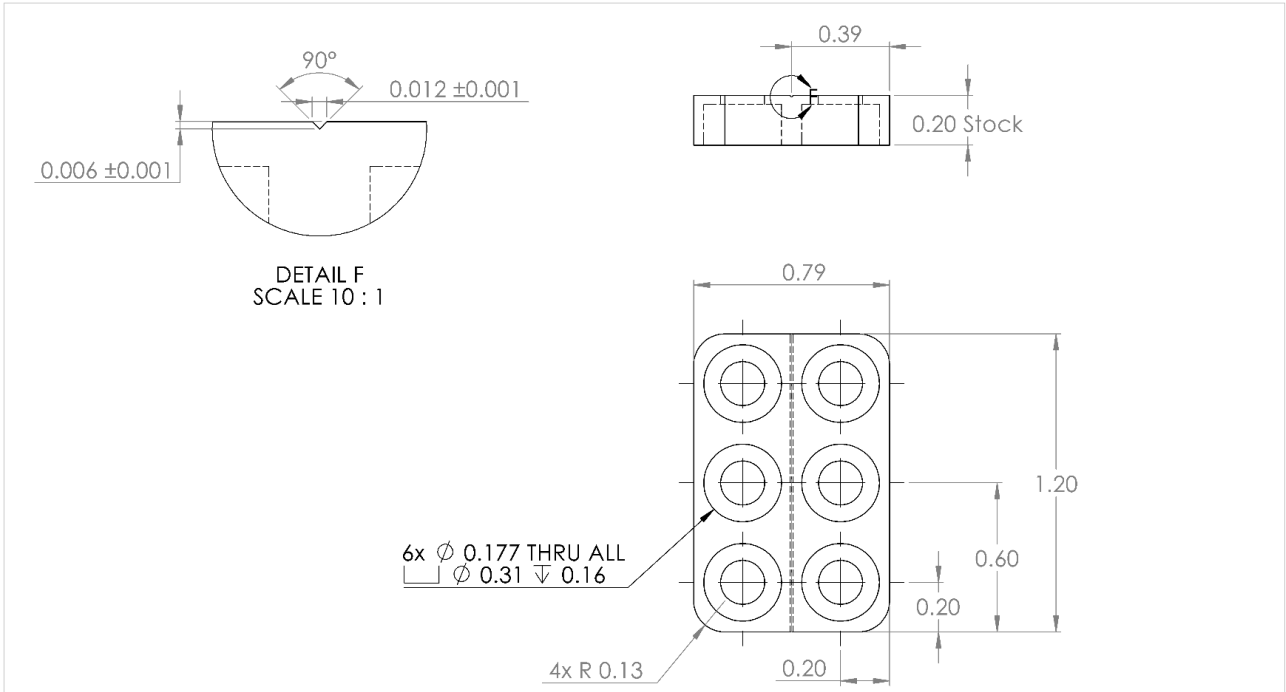

		UNLESS OTHERWISE SPECIFIED:		NAME	DATE
		DIMENSIONS ARE IN INCHES TOLERANCES: ±0.01	DRAWN	Elizabeth Buechler	10/7/16
			CHECKED		
			ENG APPR.		
			MFG APPR.		
			Q.A.		
		MATERIAL SS 316	COMMENTS: Quantity: 1		
NEXT ASSY	USED ON	FINISH			
APPLICATION		DO NOT SCALE DRAWING			

TITLE:
Sample Holder A -
Center Wire

SIZE	DWG. NO.	REV
A		

SCALE: 2:1 | SHEET 4 OF 7

5 4 3 2 1

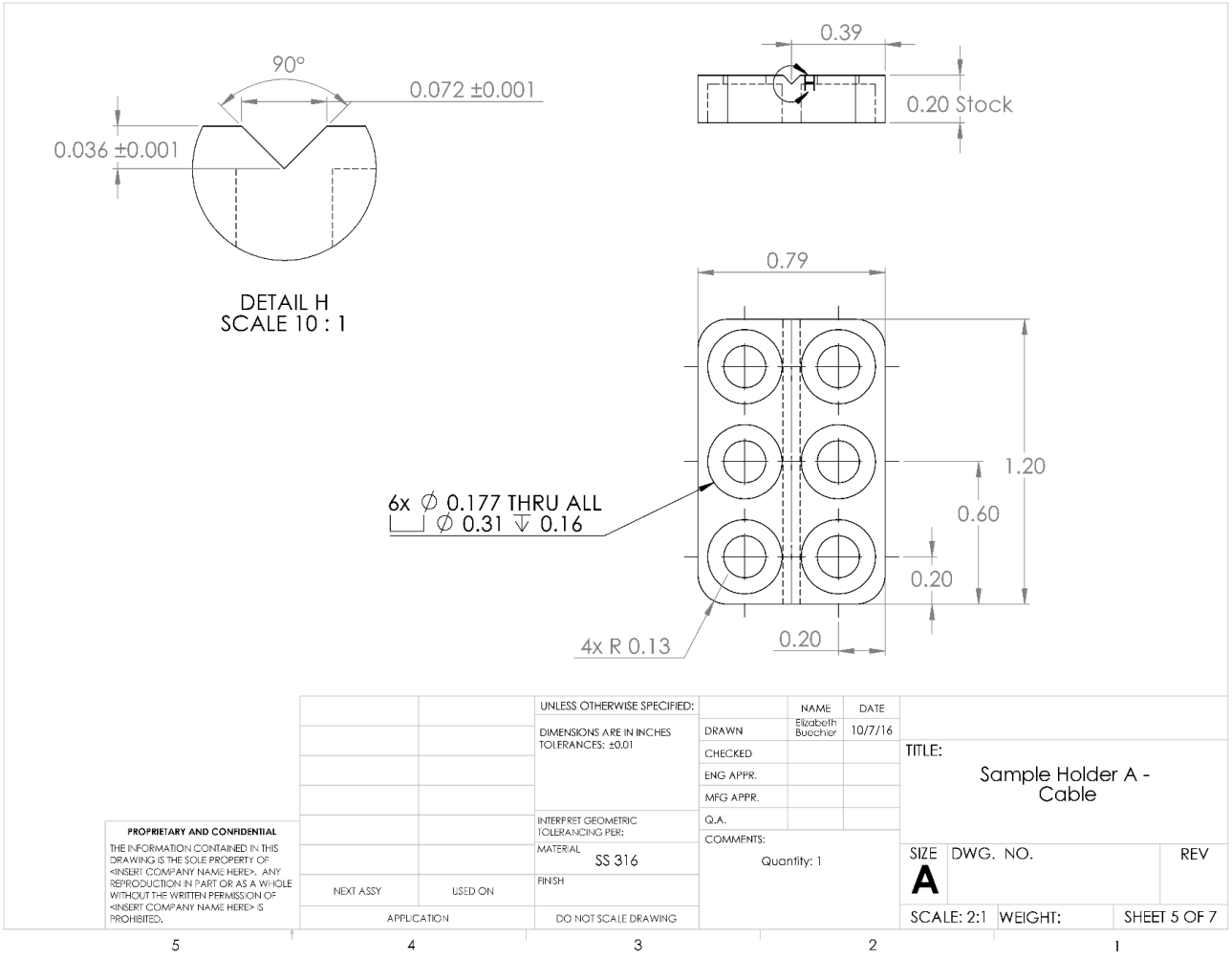

		UNLESS OTHERWISE SPECIFIED:		NAME	DATE
		DIMENSIONS ARE IN INCHES TOLERANCES: ±0.01	DRAWN	Elizabeth Buechler	10/7/16
			CHECKED		
			ENG APPR.		
			MFG APPR.		
		INTERPRET GEOMETRIC TOLERANCING PER:	Q.A.		
		MATERIAL SS 316	COMMENTS: Quantity: 1		
NEXT ASSY	USED ON	FINISH			
APPLICATION		DO NOT SCALE DRAWING			

TITLE: Sample Holder A - Cable

SIZE A | DWG. NO. | REV

SCALE: 2:1 | WEIGHT: | SHEET 5 OF 7

5 4 3 2 1

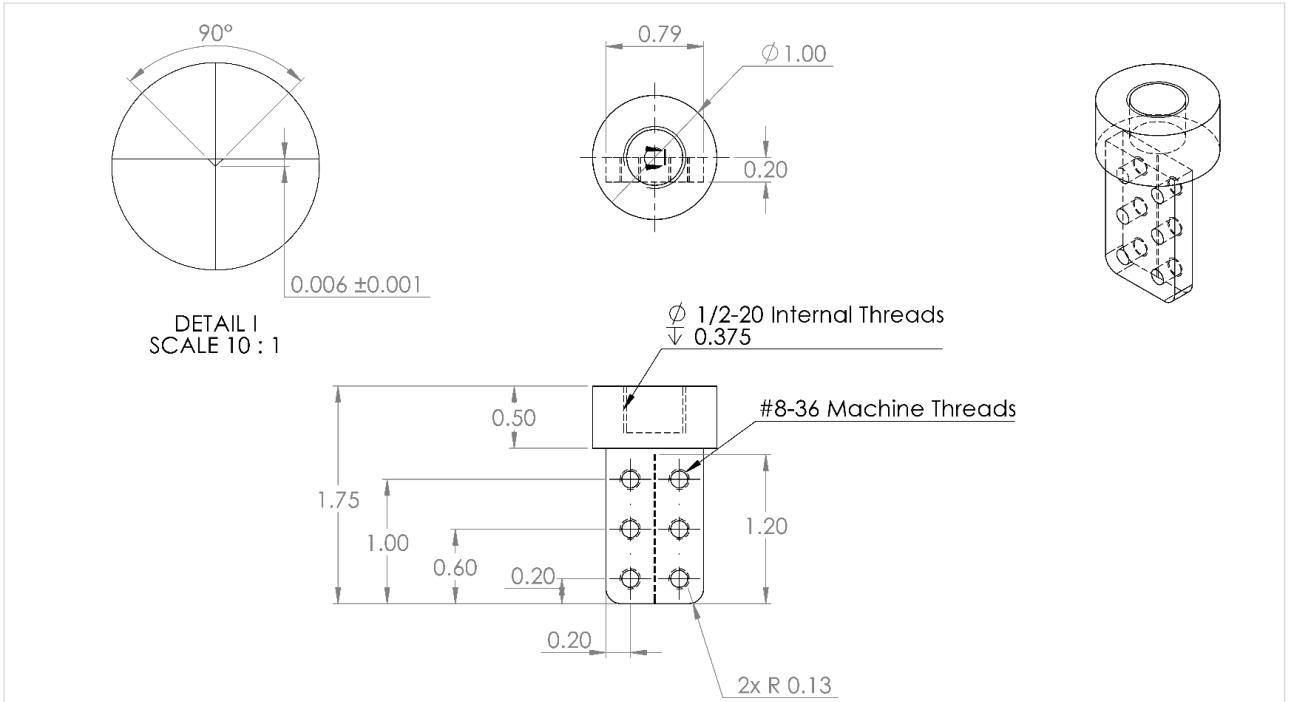

		UNLESS OTHERWISE SPECIFIED:		NAME	DATE
		DIMENSIONS ARE IN INCHES TOLERANCES: ± 0.01	DRAWN	Elizabeth Buechler	10/7/16
			CHECKED		
			ENG APPR.		
			MFG APPR.		
			Q.A.		
		MATERIAL SS 316	COMMENTS: Quantity:1		
NEXT ASSY	USED ON	FINISH			
APPLICATION		DO NOT SCALE DRAWING			

TITLE: Sample Holder D - Center Wire

SIZE A | DWG. NO. | REV

SCALE: 1:1 | SHEET 6 OF 7

5 4 3 2 1

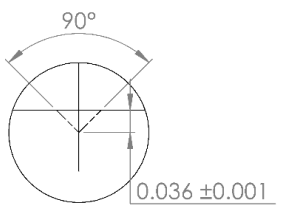

DETAIL J
SCALE 5 : 1

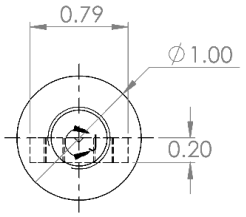

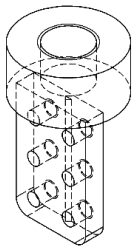

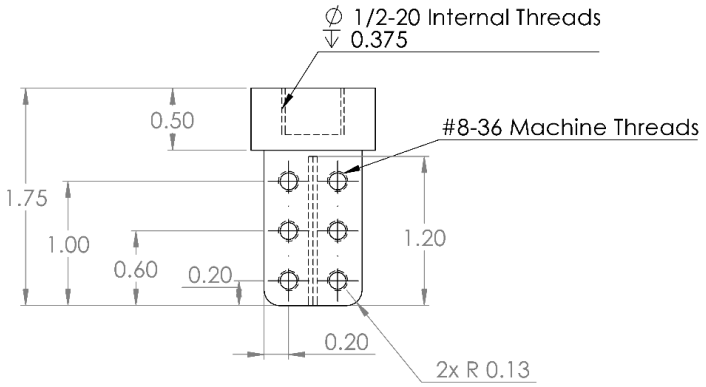

		UNLESS OTHERWISE SPECIFIED:		NAME	DATE
		DIMENSIONS ARE IN INCHES TOLERANCES: ± 0.01	DRAWN	Elizabeth Buechler	10/7/16
			CHECKED		
			ENG APPR.		
			MFG APPR.		
			Q.A.		
		MATERIAL SS 316	COMMENTS: Quantity:1		
NEXT ASSY	USED ON	FINISH			
APPLICATION		DO NOT SCALE DRAWING			

TITLE: Sample Holder D - Cable

SIZE A | DWG. NO. | REV

SCALE: 1:1 | WEIGHT: | SHEET 7 OF 7

5 4 3 2 1

8. Appendix B: Stress-Strain Plots for Mevion Samples

8.1 Reacted Strands

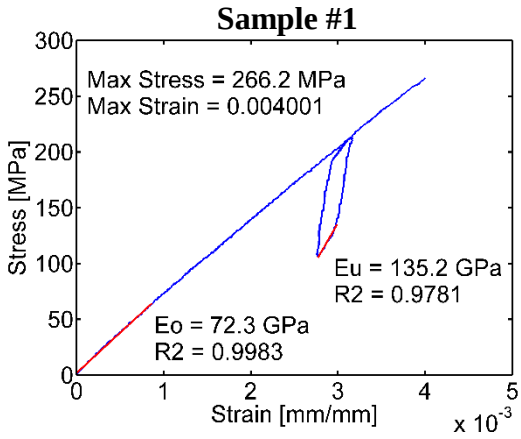

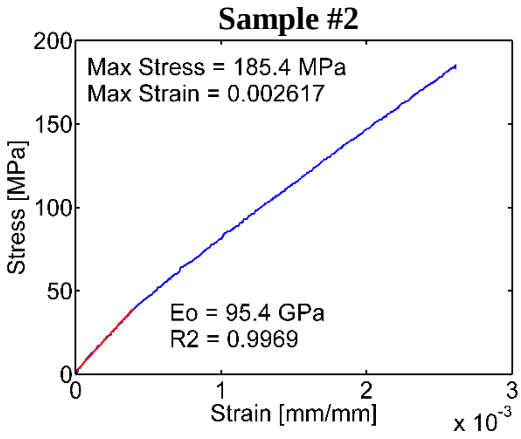

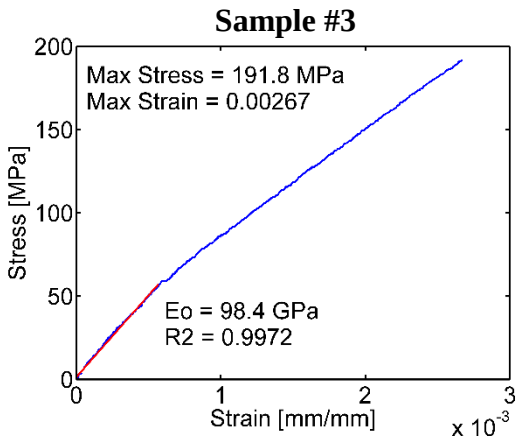

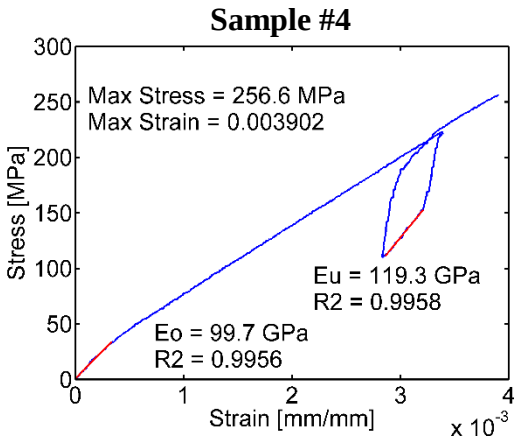

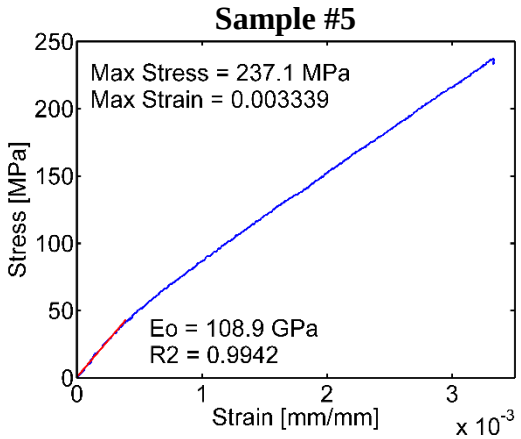

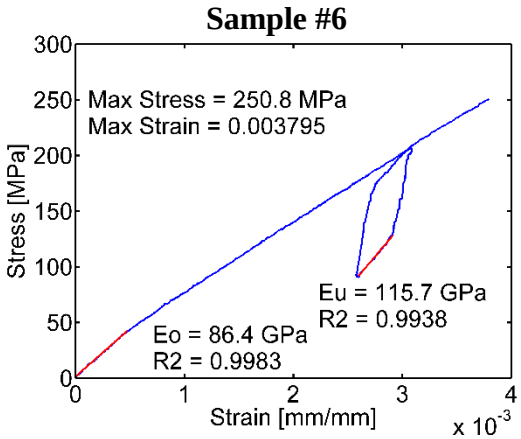

7.2 Unreacted Strands

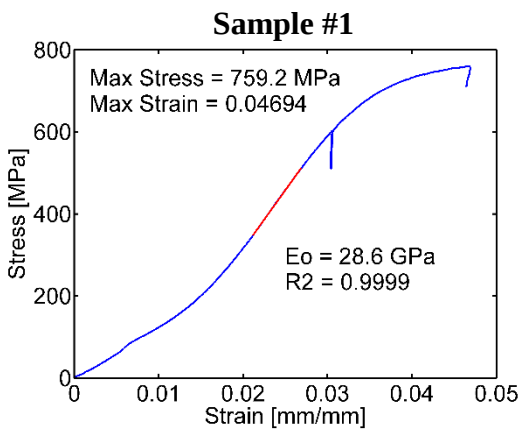

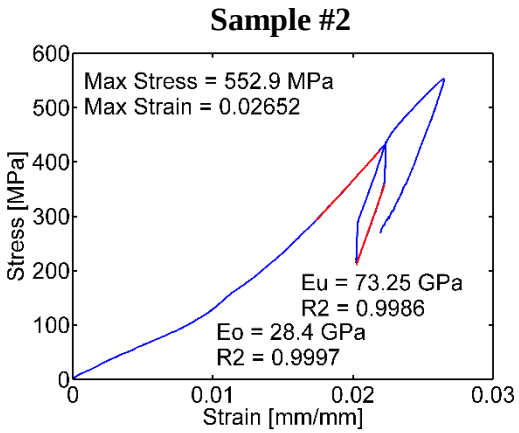

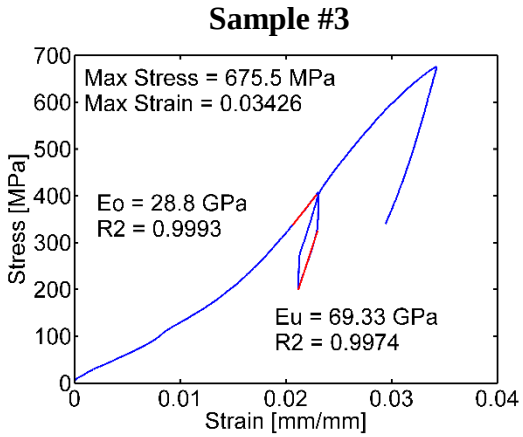

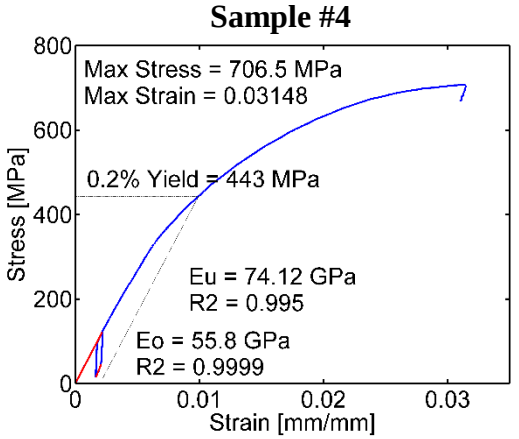

8.3 Reacted Cables

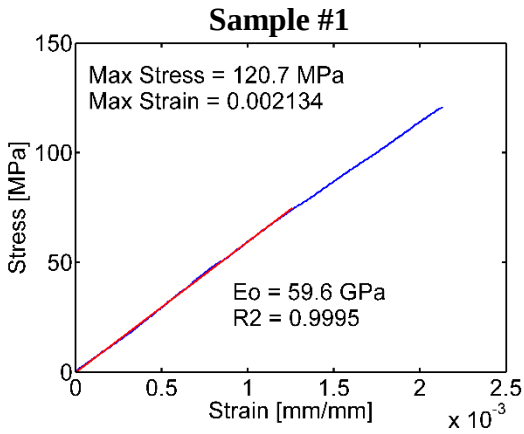

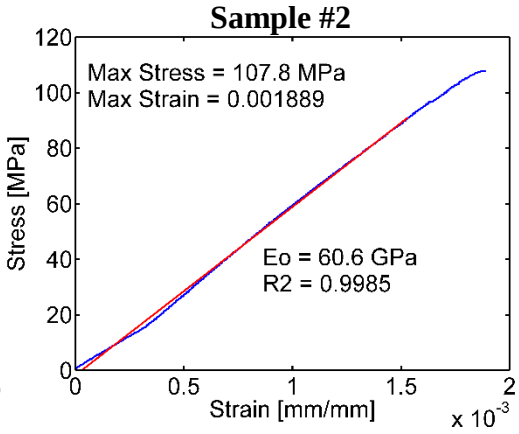

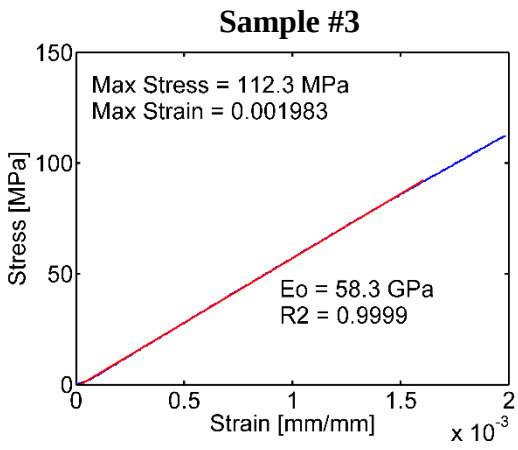
Sample #3
Max Stress = 112.3 MPa
Max Strain = 0.001983
Eo = 58.3 GPa
R2 = 0.9999
Stress [MPa]
Strain [mm/mm]
x 10^-3

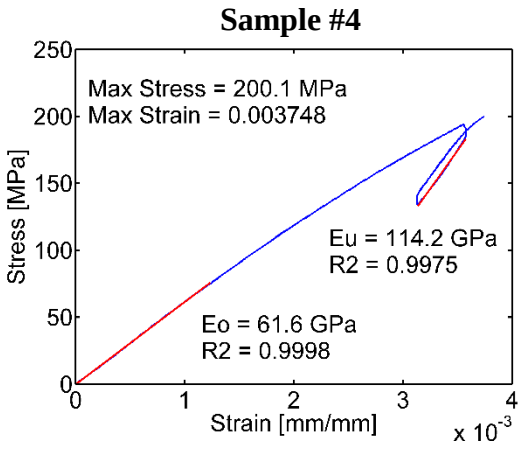
Sample #4
Max Stress = 200.1 MPa
Max Strain = 0.003748
Eu = 114.2 GPa
R2 = 0.9975
Eo = 61.6 GPa
R2 = 0.9998
Stress [MPa]
Strain [mm/mm]
x 10^-3

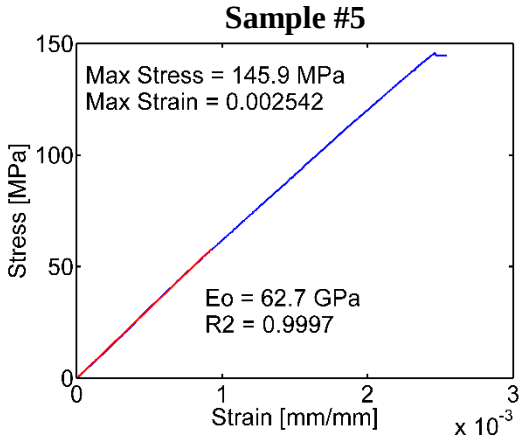
Sample #5
Max Stress = 145.9 MPa
Max Strain = 0.002542
Eo = 62.7 GPa
R2 = 0.9997
Stress [MPa]
Strain [mm/mm]
x 10^-3

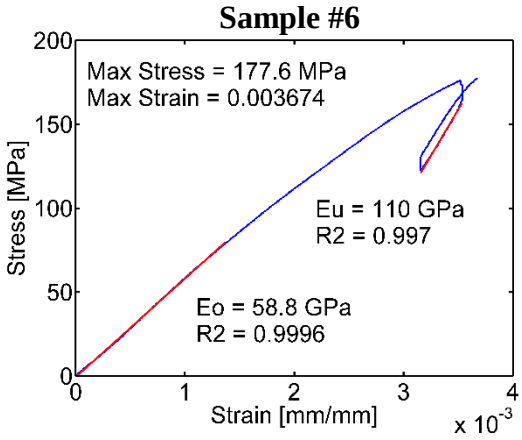
Sample #6
Max Stress = 177.6 MPa
Max Strain = 0.003674
Eu = 110 GPa
R2 = 0.997
Eo = 58.8 GPa
R2 = 0.9996
Stress [MPa]
Strain [mm/mm]
x 10^-3

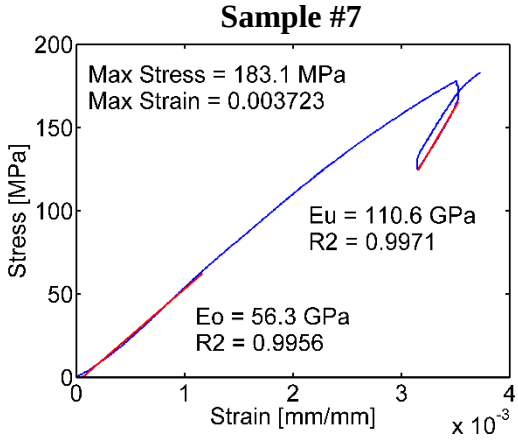
Sample #7
Max Stress = 183.1 MPa
Max Strain = 0.003723
Eu = 110.6 GPa
R2 = 0.9971
Eo = 56.3 GPa
R2 = 0.9956
Stress [MPa]
Strain [mm/mm]
x 10^-3

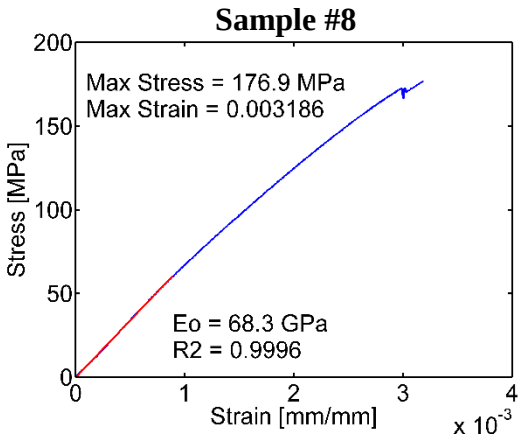
Sample #8
Max Stress = 176.9 MPa
Max Strain = 0.003186
Eo = 68.3 GPa
R2 = 0.9996
Stress [MPa]
Strain [mm/mm]
x 10^-3

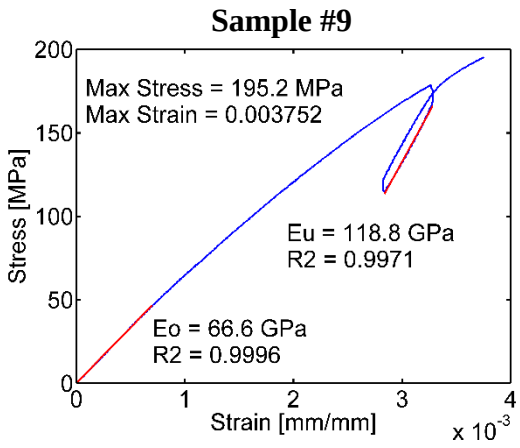

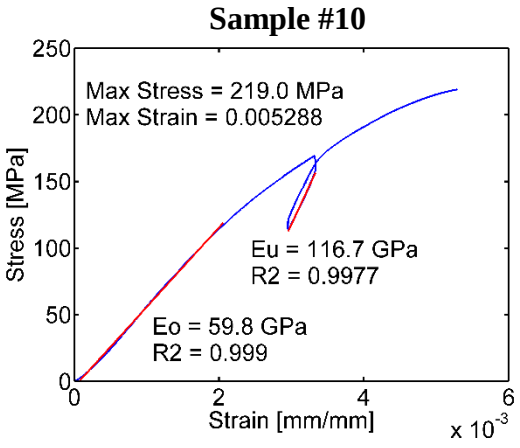

8.4 Unreacted Cables

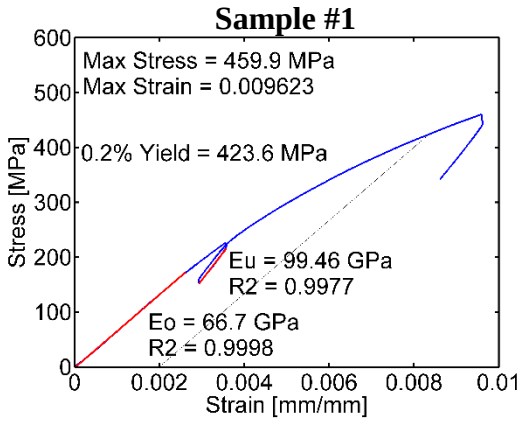

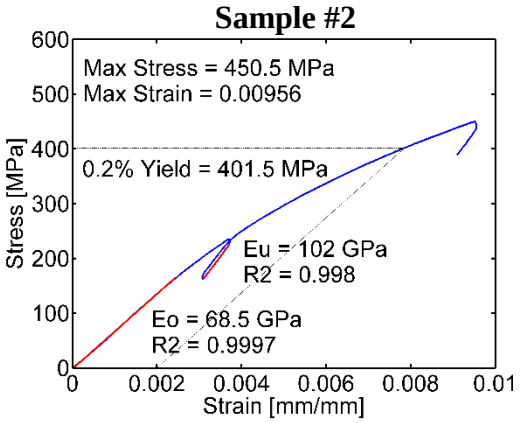

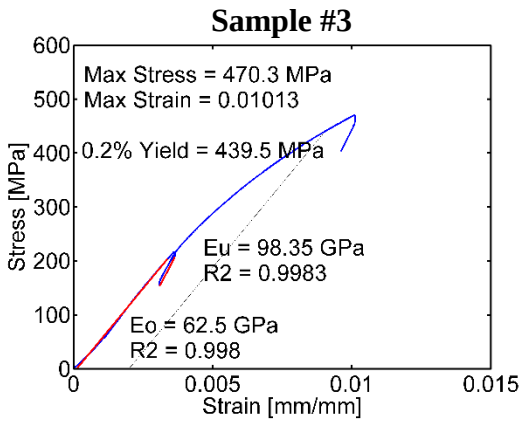

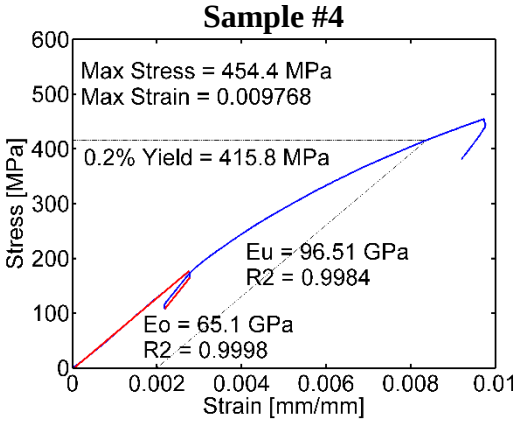

Sample #5

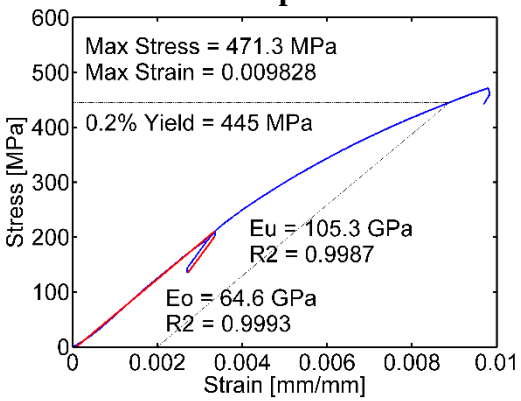

Sample #6

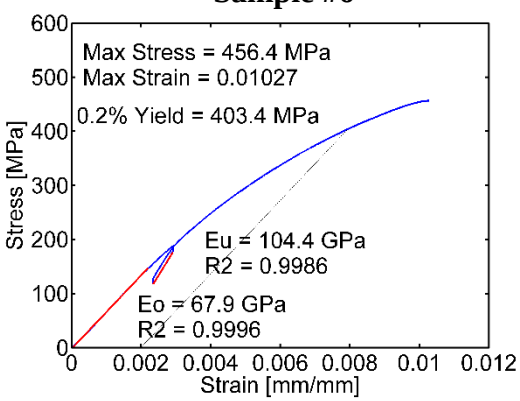

Sample #7

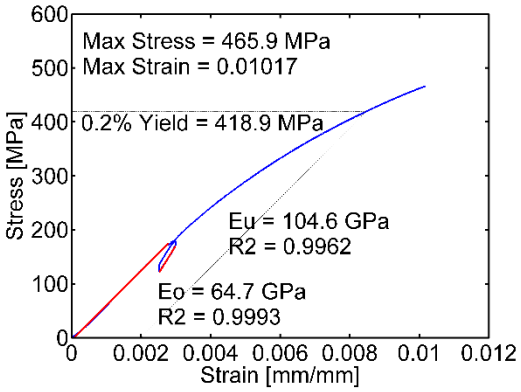

Sample #8

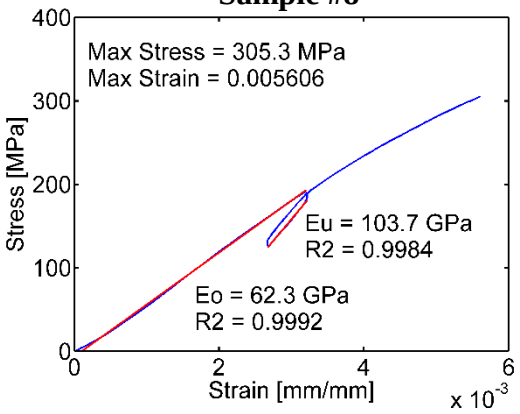

Sample #9

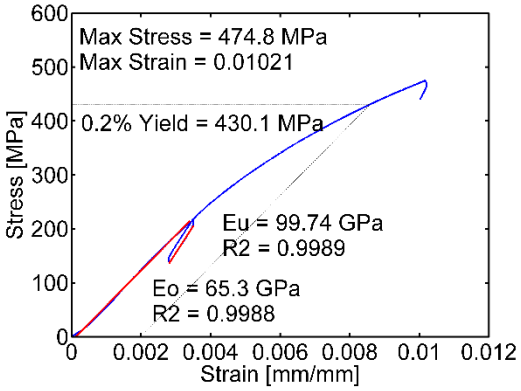

Sample #10